

RESEARCH ARTICLE

Sensory Processing

Thalamic state influences timing precision in the thalamocortical circuit

Clarissa J. Whitmire,¹ Yi Juin Liew,^{1,2} and Garrett B. Stanley¹¹Wallace H Coulter Department of Biomedical Engineering, Georgia Institute of Technology and Emory University, Atlanta, Georgia and ²Joint PhD Program in Biomedical Engineering, Georgia Institute of Technology—Emory University—Peking University, Atlanta, Georgia

Abstract

Sensory signals from the outside world are transduced at the periphery, passing through thalamus before reaching cortex, ultimately giving rise to the sensory representations that enable us to perceive the world. The thalamocortical circuit is particularly sensitive to the temporal precision of thalamic spiking due to highly convergent synaptic connectivity. Thalamic neurons can exhibit burst and tonic modes of firing that strongly influence timing within the thalamus. The impact of these changes in thalamic state on sensory encoding in the cortex, however, remains unclear. Here, we investigated the role of thalamic state on timing in the thalamocortical circuit of the vibrissa pathway in the anesthetized rat. We optogenetically hyperpolarized thalamus while recording single unit activity in both thalamus and cortex. Tonic spike-triggered analysis revealed temporally precise thalamic spiking that was locked to weak white-noise sensory stimuli, whereas thalamic burst spiking was associated with a loss in stimulus-locked temporal precision. These thalamic state-dependent changes propagated to cortex such that the cortical timing precision was diminished during the hyperpolarized (burst biased) thalamic state. Although still sensory driven, the cortical neurons became significantly less precisely locked to the weak white-noise stimulus. The results here suggests a state-dependent differential regulation of spike timing precision in the thalamus that could gate what signals are ultimately propagated to cortex.

NEW & NOTEWORTHY The majority of sensory signals are transmitted through the thalamus. There is growing evidence of complex thalamic gating through coordinated firing modes that have a strong impact on cortical sensory representations. Optogenetic hyperpolarization of thalamus pushed it into burst firing that disrupted precise time-locked sensory signaling, with a direct impact on the downstream cortical encoding, setting the stage for a timing-based thalamic gate of sensory signaling.

burst; coding; optogenetic; thalamocortical; vibrissa

INTRODUCTION

Sensory thalamus plays a critical role in gating information flow from sensors in the periphery to cortex, ultimately shaping how we perceive the world. Importantly, thalamic gating properties are not static but instead vary dynamically through a range of modulatory mechanisms, including local membrane and synaptic properties (1), stimulus history (2), and neuromodulatory inputs (3, 4). Although arising from different mechanisms, these modulatory inputs have the net effect of altering the baseline membrane polarization level in the thalamus, referred to here as “thalamic state,” which plays an important role in determining the encoding properties of the thalamic neurons that serve as primary inputs to sensory cortex. Perhaps most prominently, modulation of the baseline membrane potential in thalamic neurons

enables distinct tonic and burst firing modes due to the selective engagement of low threshold calcium channels during prolonged hyperpolarization (5). It has long been posited that these two firing modes could dynamically control information processing (6), but the precise way in which this could happen has remained speculative and the way in which cortical coding properties are shaped is unknown.

Although the large majority of studies of T-type calcium channel bursts in thalamus have been focused on the underlying detailed biophysical mechanisms enabled by brain slice recordings, there have been a number of investigations of the intact circuitry in vivo. At the thalamocortical synapse, in vivo studies have shown that spontaneous burst spikes are more effective at driving cortical spiking (7) and evoke larger cortical depolarizations (8) than tonic spikes. The in vivo properties of burst and tonic spiking have been

explored perhaps most extensively in the visual pathway (9–13), with burst firing shown to be reliably elicited across trials in response to visual stimulation (11, 13, 14), associated with an “all-or-none” type of response to facilitate detection of changes in the visual scene (11, 15) consistent with mechanisms that would serve as a “wake-up call” to cortex (6) for salient stimuli (16). Furthermore, although historically controversial, it has been shown in a number of studies that thalamic bursting is not just observed in sleep states or under anesthesia but is present, albeit reduced, in the awake brain (2, 17, 18). However, the implication for downstream cortical encoding remains elusive because of the complexity of the thalamocortical circuitry. It has been estimated that 50–100 thalamic neurons converge as the primary drivers of a single cortical neuron (8), where the concerted effort of a relatively large number of synaptic inputs is needed to drive supra-threshold cortical activity. Without a mechanism to manipulate the population activity of thalamic neurons converging on a common cortical target independent of the sensory drive, the role of tonic/burst firing in driving downstream cortical activity remains elusive.

In this study, we used a combination of extracellular electrophysiological recordings in the ventral posteromedial (VPm) thalamus and primary somatosensory cortex (S1) and inhibitory optogenetic manipulation of thalamic state in the vibrissa pathway of the anesthetized rat to determine the role of thalamic state on sensory signaling in the pathway. Specifically, a spike-triggered analysis was implemented in response to a weak, sensory white-noise whisker stimulus that captures both the sensory feature selectivity and overall sensitivity of the neural activity to sensory drive (19–21). We found that tonic thalamic spiking was precisely time locked to the sensory stimulus, exhibiting sensitivity to rapid transients in the sensory input over 10–15 ms, consistent with previous studies (20). However, we found that burst spiking in VPm, while strongly driven by sensory input, exhibited timing variability that disrupted spike-triggered feature selectivity for both bursting in the baseline condition, and optogenetically induced burst mode. In S1, when the thalamus was dominated by tonic firing (i.e., without thalamic hyperpolarization), cortical neurons exhibited similar feature selectivity as observed in VPm. However, when the thalamus was optogenetically hyperpolarized, the cortical spike-triggered analysis revealed a reduction in precise stimulus-locked spiking in S1 units in response to the white-noise whisker stimulus, yet maintained a consistent overall stimulus-driven firing rate. Given the sensitivity of the cortex to precise timing of thalamic projection neurons, these results suggest that shifts in thalamic state disrupt precise timing of thalamic inputs to cortex that weaken the potency of the thalamic bursts for weak sensory inputs, setting the stage for a timing-based gating of information flow to cortex that determines what signals do and do not get transmitted.

METHODS

Experimental Procedures

Acute surgery.

All procedures were approved by the Georgia Institute of Technology Institutional Animal Care and Use Committee

and were in agreement with guidelines established by the National Institutes of Health. Nineteen female albino rats (Sprague–Dawley, 250–300 g) were anesthetized intravenously using a fentanyl cocktail [fentanyl (5 µg/kg), midazolam (2 mg/kg), dexmedetomidine (150 µg/kg)]. A craniotomy was performed over VPm (2–4 mm caudal to bregma, 1.5–3.5 mm lateral to the midline), and in a subset of animals, a second craniotomy was performed over S1 (1–3 mm caudal to bregma, 4.5–6 mm lateral to the midline). At the termination of the experiment, the animal was euthanized with an overdose of sodium pentobarbital (euthasol, 0.5 mL at 390 mg/mL). All optogenetically transfected animals that underwent cortical probe recordings were perfused, and their brains were imaged for verification of opsin location and cortical probe location.

Electrophysiology.

Tungsten microelectrodes were lowered into the thalamus (depth: 4.5–6 mm) using a micropositioner (Kopf, Luigs-Neumann). Multielectrode probes (A1x32-10mm-50-177, NeuroNexus) were lowered perpendicular to S1 (45° relative to vertical; depth: 2 mm). The topographic location of the electrode was identified through manual stimulation of the whisker pad. If the unit demonstrated responsiveness to multiple whiskers, it was not recorded and the electrode continued to be advanced until a new whisker sensitive unit was isolated. Upon manual identification of the single primary whisker for the recorded unit(s), the primary whisker was threaded into the galvo motor to permit stimulation of a single whisker. For thalamic recordings, a punctate adapting whisker stimulus (9 punctate stimuli at 6° amplitude or 2,230°/s at 100-ms interval) was applied to measure the first spike latency shift. If the first spike latency shift for the last punctate stimulus was greater than 20 ms relative to the first punctate whisker stimulus, the unit was classified as being within the nearby posteromedial (POm) complex of the thalamus (22) and was therefore not recorded.

Sensory stimulus.

Mechanical whisker stimulation was delivered using a precisely controlled galvo motor (Cambridge Technologies, custom Matlab software). The mechanical stimulus applied to the whisker in the rostral-caudal direction consisted of sensory white noise (low pass filtered at 200 Hz, standard deviation of the noise was 0.6° or 223°/s). Feedback from the whisker stimulator for unfrozen white-noise segments were used for further spike-triggered analysis across all units in VPm and S1 (down sampled to 4.88 kHz). In all cortical recordings, in addition to the unfrozen white-noise segments, 4-s segments of frozen white noise were presented 100–150 times per recording. Frozen white-noise segments were used to compute across trial reliability, here measured as trial-to-trial jitter (23).

Viral transfection procedure.

All surgical procedures followed sterile protocol. A small craniotomy was made above VPm (3 mm lateral, 3 mm caudal to bregma). A 10-µL syringe (Neuros Syringe, Hamilton, Inc) filled with the virus (rAAV5-CamKIIa-Jaws-KGC-GFP-ER2 or rAAV5-CamKIIa-eNpHR3.0-EYFP, UNC Viral Vector Core Services) was lowered to depth of 5.2 mm before injecting

1 μ L of virus at a rate of 0.2 μ L/min (iSi system, Stoelting). The syringe remained in place for 5 min after the injection was complete to allow the virus to diffuse. Opsin expression was fully realized at 2–3 wk postsurgery. The CamKIIa promoter was used to target an inhibitory opsin (24) into excitatory neurons (25) in the thalamus. Although this promoter would prohibit the expression of the opsin in the neighboring thalamic reticular nucleus, it would not preclude expression in nearby whisker sensitive thalamic nuclei such as the posterior medial nucleus (POm). However, the optical fiber was physically coupled to the electrode which was located in the VPM. Given the dorsal positioning of POm relative to VPM, the direction of optical activation downward into the tissue would further restrict optogenetic effects to the VPM relative to POm.

Optogenetic stimulus.

Optical manipulation was administered with a controlled pulse of light through a custom optrode consisting of an optical fiber (200 μ m diameter; Thorlabs) and an electrode (Tungsten microelectrode; Frederick Haer & Co., Bowdoinham, ME) that was lowered into the VPM. Upon identifying a whisker sensitive cell, light sensitivity was assessed by the postinhibitory rebound spiking response using a train of 250 ms light pulses ($\lambda = 590$ or 617 nm for Halorhodopsin and Jaws, respectively). The whisker was then stimulated without (baseline) and with (hyperpolarized) light provided directly to the thalamus [maximum intensity of 1.6 mW as measured with a power meter; estimated 50 mW/mm² at the fiber tip given a 200- μ m-diameter fiber (cross-sectional area of 0.0314 mm²)]. Studies that have directly quantified the effects of optical stimulation on local tissue heating and neural activation (in the absence of opsin expression) have found no significant difference in the firing rate change for 1-mW light intensity (26) or minor firing rate changes for 3-mW light intensity but no behavioral effects (27). Optogenetic stimulus conditions (light on/hyperpolarized, light off/baseline) were interleaved to avoid long-term adaptation effects.

Analytical Methods

Spike sorting.

Spike sorting for single-channel recordings was performed online and validated offline using Waveclus (28). Spike sorting for multichannel electrodes was performed offline using the KlustaKwik software suite (29). Isolation of the unit was confirmed by the waveform amplitude (specifically that the ratio of the peak-to-peak voltage of the mean waveform divided by the standard deviation of the waveform was greater than 3) and the absence of spikes in the absolute refractory period as revealed by the interspike-interval distributions (VPM: mean of 0.22%, S1: mean of 0.38% of spikes in absolute refractory period of 1 ms). Cortical units were further classified as putative fast spiking if the peak-to-trough duration was less than 0.4 ms, and regular spiking otherwise (30). For the data analyzed here, 25 of 32 cortical units were classified as fast spiking units.

Burst spike classification.

Burst spikes were classified here from the extracellular recordings as two or more spikes with an interspike interval

of less than 4 ms with the first spike in the burst preceded by 100 ms of silence (12).

Spike-triggered analysis.

Spike-triggered analysis for exploration of feature selectivity has been utilized widely in the thalamocortical circuit of the visual (11, 31–33), auditory (34, 35), and somatosensory pathways (19–21, 36). Here, we implemented spike-triggered analysis for each unit recorded in VPM thalamus and S1 cortical layer 4. Specifically, feature selectivity was first estimated for each recorded unit using a simple spike-triggered average (STA) (37).

$$STA = \frac{1}{N} \sum_j s(t_j) \quad (1)$$

where N is the number of spikes and s is the stimulus segment in a window surrounding each spike (–30 to +5 ms). Note that the collection of stimulus sequences preceding each spike in a data set is referred to here as the “spike-triggered ensemble,” where the spike-triggered average is the average of this ensemble. To evaluate the potential differences between signaling properties for tonic and burst firing, the spike-triggered averages were computed in two different ways. First, the burst- and tonic-triggered averages were computed from burst and tonic spikes, respectively, where spikes were classified as “tonic” or “burst” based on the above classification rules. In this case, the tonic-triggered average was computed exclusively from tonic spikes, and the burst-triggered average was computed exclusively from burst spikes. Second, in contrast, the baseline/hyperpolarized condition triggered averages were computed from all spikes in a given optogenetically manipulated condition. Although the baseline condition contained more tonic spikes and the thalamic hyperpolarized condition contained more burst spikes, the conditions are not exclusively burst or tonic spikes. Thus, these triggered averages were more reflective of the gross signaling properties of the condition of the thalamus (baseline versus hyperpolarized). The bootstrap estimate of the confidence intervals on the spike-triggered average was computed as the ± 2 standard deviation of the shuffled STA distribution across 500 repetitions (37). Note that we implemented multiple techniques of estimating the feature selectivity of the neurons including spike-triggered covariance (STC), generalized linear models, and nonlinear-input models (19, 38). The results were qualitatively consistent across all methods employed, so we implemented spike-triggered average analysis throughout the study due to its simplicity. STC analysis of both VPM and S1 neurons did not reveal significantly different structure for the neurons recorded under our experimental conditions as compared with STA, and are thus not shown here. More importantly, STC analysis did not reveal a shift in feature selectivity across thalamic states, consistent with the STA analysis presented here.

Signal-to-noise ratio of the spike-triggered average.

The signal-to-noise ratio of the recovered STA (SNR_{STA}) was quantified as the peak-to-peak amplitude of the STA (STA_{PP}) within 10 ms of the spike (where the significant filter activity is contained) divided by the peak-to-peak amplitude of the STA from 30 to 20 ms before the spike (STA_{noise} ; where there

is no expected filter information). An SNR value of 1 means the amplitude of the STA near the spike time is not different from the amplitude of the noise fluctuations. Therefore, any units with an SNR value less than 2.5 were excluded from further analysis.

Principal component analysis.

There was significant diversity in the resultant STA structure across recorded neurons and across animals. Utilizing the approach of Estebanez et al. (19) to make comparisons of the feature selectivity across the population of recorded neurons, we conducted a principal components analysis of the recovered STA across all recorded neurons. The analysis computes the eigenvalues (percent variance explained) and eigenvectors (principal components). Importantly, the analysis seeks to identify the principal components that account for a majority of the variability in the input. If the input data can be represented by only a few principal components, this suggests that most of the information in the data set can be represented in a lower dimensional space. Here, we found that the first two principal components computed from the recovered STA across all recorded neurons accounted for the majority of the variance (71.8% VPm, 78.4% S1), and therefore were interpreted as representative of the primary structure in the sensory input relevant for spiking in the population.

Spiking nonlinearity.

A linear-nonlinear model proposes that the incoming sensory stimulus (*s*) is linearly filtered with the feature selectivity of the particular neuron (here defined as the STA) to generate the filtered stimulus. Mathematically, the filtered stimulus (*y*) is the convolution of the stimulus (*s*) and the feature selectivity of the unit (tSTA) (39). In this linear-nonlinear model, the linearly filtered stimulus (*y*) is then passed through a point nonlinearity [*P*(spike|*y*)] which produces an estimate of the firing rate given the sensory stimulus. This point nonlinearity simply maps the filtered stimulus occurrence to the probability of the neuron firing. The nonlinearity [*P*(spike|*y*)] was estimated as the ratio of the probability of spike-triggered stimuli [*P*(*y*|spike)] to the probability of any stimulus segment in the stimulus [*P*(*y*)] multiplied by the mean firing rate of the neuron [*P*(spike)] (37):

$$p(\text{spike}|y) = p(\text{spike}) \frac{p(y|\text{spike})}{p(y)} \tag{2}$$

Because the slope of the static nonlinearity is determined by the separation between the spike-triggered ensemble and the Gaussian distributed white noise, as the spike-triggered ensemble distribution becomes more selective (i.e., the mean moves away from the filtered stimulus distribution), the separability of the distributions increases, and the slope of the nonlinearity also increases. Intuitively, this means that the shape of the nonlinearity gives an estimate of the separability of the spike-triggered ensemble and the stimulus distribution, or how strongly tuned a neuron is for that particular feature, given by the STA. A steeper slope in the nonlinearity suggests a stronger tuning than a shallower slope. As with the STA analysis, to evaluate the potential differences between the nonlinearity for tonic and burst firing, we analyzed the nonlinearity in two different ways. First, we assessed the nonlinearity for the tonic and burst spikes,

where the nonlinearity estimates were generated exclusively from tonic or burst spikes. Second, we assessed the nonlinearity from all spikes in a given optogenetically manipulated condition. Again, although the baseline condition contained more tonic spikes and the thalamic hyperpolarized condition contained more burst spikes, the conditions are not exclusively burst or tonic spikes. Thus, these nonlinearities were more reflective of the gross properties of the condition of the thalamus (baseline vs. hyperpolarized). For all analyses, the best estimate of the STA was defined as tonic spike-triggered average for thalamic units and the baseline thalamic state (i.e., not optogenetically manipulated) for the cortical units. Throughout the manuscript, we separate the firing rate [*p*(spike)] from the shape of the nonlinearity [*p*(*y*|spike)/*p*(*y*)] to avoid confounding differences in firing rate with differences in tuning.

STA jitter.

When providing a punctate whisker stimulus, computing a metric such as first spike latency and jitter in the first spike latency is straightforward given the precise onset of the stimulus. However, estimation of the jitter in response to a weak sensory white-noise stimulus is more complicated due to different timing variability for different sensory features and differing feature selectivity across neurons (40). There is no clear onset of the sensory stimulus (as it is ongoing) and there is no repeatability in unfrozen white-noise segments (where the unfrozen white-noise data collection was necessitated by the STA analysis). Therefore, to estimate the temporal jitter in the thalamic firing in response to unfrozen white-noise segments, we developed a metric (τ_{jitter}) to estimate the time of each recorded spike relative to when we would predict a spike based on the spike-triggered average. τ_{jitter} is defined for each spike as the temporal lag (t_{lag}) for the peak correlation between the STA and the stimulus segment surrounding that spike (−30 ms to +5 ms):

$$\tau_{jitter} = \arg \max_{t_{lag}} correlation(STA, s(t_j))$$

For a recording, this analysis thus results in a distribution of τ_{jitter} values across the recorded spikes. The τ_{jitter} distribution was normalized by the total number of spikes in each condition to create a probability distribution (tonic/burst spikes, baseline/hyperpolarized optogenetic conditions). It is important to note that although this is an indirect measure of timing variability that carries with it the assumption of an underlying feature selectivity, for the cortical recordings where we had collected significantly more responses to frozen white noise, we validated this approach using more traditional means of timing variability analysis, finding similar metrics of timing precision/jitter (see below).

Precision.

The precision in the sensory white-noise-evoked firing was estimated for tonic and burst spiking, as well as for the baseline and hyperpolarized conditions, based on the τ_{jitter} distribution described above. The precision was defined as the number of spikes with τ_{jitter} values of ±1-ms duration normalized by the total number of spikes, or the area under the τ_{jitter} distributions between ±1 ms (denoted by gray shaded bars in Fig. 4C).

Trial-to-trial jitter.

In the cortical units, frozen white-noise segments were recorded. Frozen white-noise segments enable the direct assessment of across trial variability in the evoked neural activity. Here, we followed the methodology of Montemurro et al. (23) to compute a trial-to-trial variability metric. First, a peristimulus time histogram was computed with 1-ms resolution. The maximum firing rate was identified for each neuron and a threshold was set at 0.5 times the maximum firing rate. All peaks in the peristimulus time histogram (PSTH) that exceeded this threshold were extracted and aligned to create an event-triggered average which was parameterized using a Gaussian function. The standard deviation of the Gaussian fit was defined as the trial-to-trial jitter. Neurons with fewer than 200 spikes in the event aligned PSTH were excluded from the analysis due to poor Gaussian fit (2 of 32 neurons).

Statistical comparisons.

All pairwise statistical comparisons were computed using a Wilcoxon signed-rank test unless otherwise noted.

RESULTS**Spike-Triggered Analysis in the Thalamus and Cortex**

We recorded thalamic and cortical extracellular spiking activity in response to sensory white-noise stimulation of a single whisker in the vibrissa pathway of the fentanyl-cocktail anesthetized rat to enable long-duration, controlled measurements needed for precise estimates of feature selectivity (Fig. 1A, see METHODS). We estimated the feature selectivity for each unit as the spike-triggered average (STA), which captures the features of the sensory stimulus that tended to precede spiking (see METHODS). Spike-triggered analysis has been widely utilized in studying feature selectivity in the visual (11, 31–33), auditory (34, 35), and somatosensory (19–21, 36, 41–43) pathways. Although this quantification relied on longer unique noise segments and thus much of the data collection was focused on this, in a small subset of neurons we also recorded the response to short (4–10 s) frozen white-noise segments to examine the response across trials. Figure 1B shows an example recording from a simultaneously recorded pair of neurons in topographically aligned regions of the thalamus (left column, ventral posteromedial nucleus, VPM) and cortex (right column, primary somatosensory cortex, S1) in response to the repeated presentation of a single frozen white-noise segment (top of each column). Across trials, the repeatability of the response to the noise stimulus is apparent in the VPM raster plot, with clear vertical patterns across trials. The spike-triggered average (STA) was computed for the thalamic and cortical unit for stimulus segments from –30 ms before the spike to +5 ms afterwards at a 0.2-ms resolution (Fig. 1C) from the long unfrozen white-noise segments. The VPM STA on the left shows clear feature selectivity in the 10–15 ms before the thalamic spike as evidenced by the large amplitude of the STA relative to the shuffled case (gray confidence intervals). Beyond 15 ms before the spike, the VPM STA is essentially flat and within the confidence bounds on the shuffled process. This suggests that, on average, the thalamic unit is only sensitive to the stimulus occurring in the previous 10–15 ms. The S1 unit also

displays feature selectivity as evidenced by the shape and amplitude of the S1 STA immediately before the cortical spike relative to the shuffled case, shown on the right in Fig. 1C. Although the VPM STA is nearly 10 times as large in amplitude as the S1 STA (note the relative sizes of the scale bars), the similarity in the temporal dynamics can be visualized by scaling and shifting the VPM STA by 2 ms relative to the S1 STA (Fig. 1C, bottom, S1 STA black, VPM STA shifted by 2 ms and scaled by a factor of 0.1 as gray dashed line). Together, this suggests that after accounting for synaptic delay, the S1 neuron is time-locked to the same basic feature in the single whisker sensory stimulus as the VPM neuron, but the reduction in magnitude means that it is less consistently responsive to this feature.

Although this simple comparison provides an interesting observation for a single pair of topographically aligned neurons, we also made comparisons of the feature selectivity across the population of recorded neurons in thalamus and cortex through this STA analysis. First, we visualized the shape of the spike-triggered average for a sample of example thalamic and cortical units (Fig. 1D). These STA filters for each neuron cannot be simply averaged together to give an estimate of the feature selectivity of the population of neurons due to differences in the phase and directionality of the recovered STA across different recorded units. Instead, utilizing an approach from Estebanez et al. (19), we performed a principal component analysis on the set of recovered thalamic and cortical STA filters across each individual unit to identify salient filter properties that generalized across the population of recorded units (Fig. 1E). Importantly, this provides generalization across neurons within the same animal, and across animals/experiments. The first two principal components for the spike triggered averages of both thalamus and cortex explain the majority of the variance for the set of recovered filters, similar to what has been seen previously for cortex (19). Furthermore, a simple time shift of 2.5 ms for the VPM principal components relative to the S1 principal components (Fig. 1F, dashed lines shows time-shifted VPM STA) to account for the synaptic delay demonstrates the similarity in the STA subspace spanned by these principal components. It seems that despite not necessarily being recorded simultaneously or even in the same animal, there is a high degree of overlap in the low dimensional subspace of feature selectivity for thalamocortical neurons in the whisker pathway. Note that we further analyzed the spike-triggered covariance (STC) for the same data and found that the subspace spanned by the recovered linear filters matched the subspace estimated using the linear filters recovered using STA, thus not revealing any higher order feature selectivity in the data.

Tonic and Burst Spike-Triggered Analysis in Thalamus

Inherent in the spike-triggered analysis, however, is an assumption that the average filter is representative of the sensory stimulus preceding all spikes (44), treating all spikes as the same. Yet neurons in the thalamus are well known for exhibiting two fundamentally different types of firing: tonic spiking and burst firing mediated through T-type calcium channels (5). Burst spikes were classified here from the extracellular recordings as two or more spikes with an

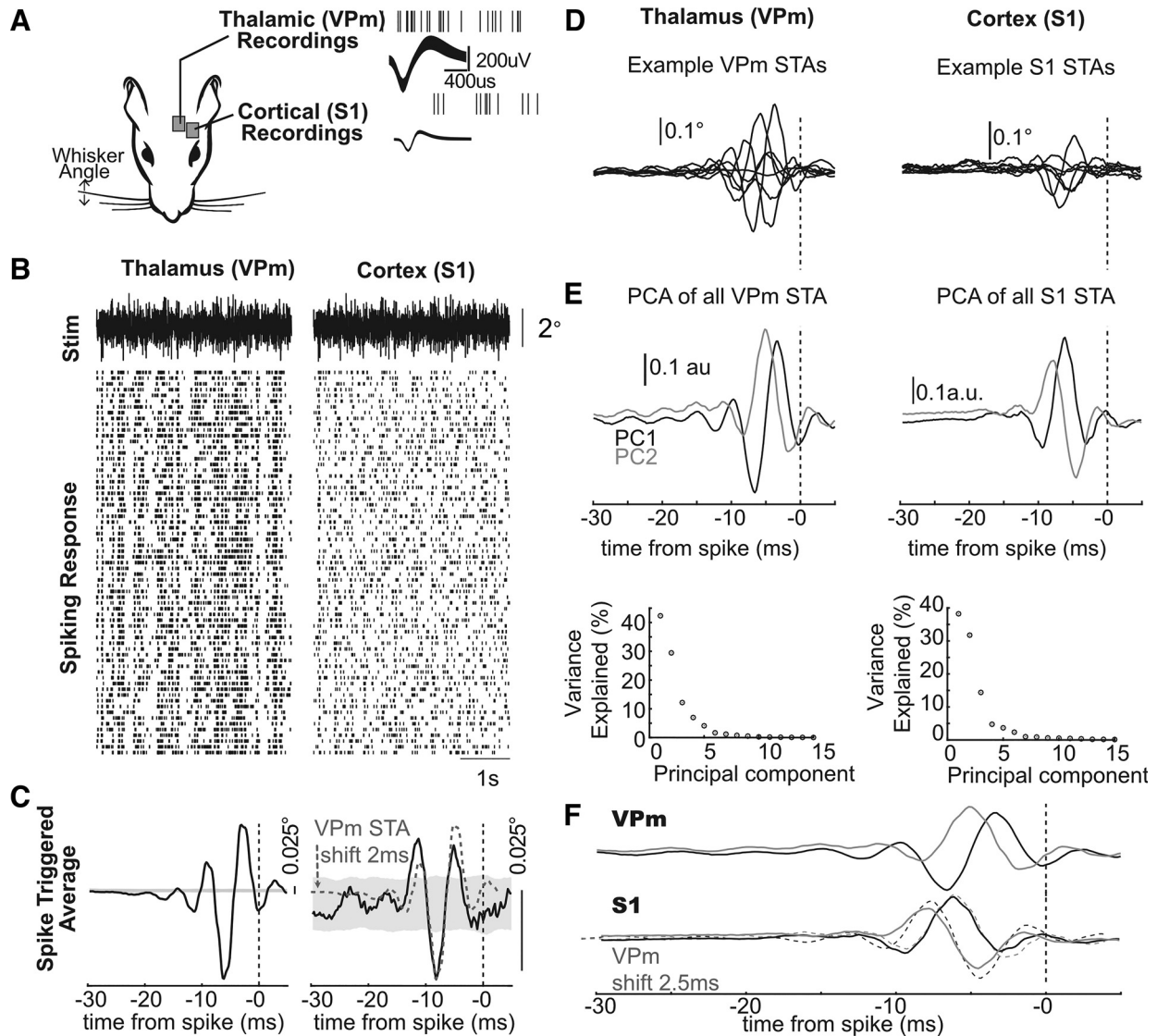


Figure 1. Spike-triggered analysis in the thalamocortical circuit of the rat whisker pathway. *A:* experimental paradigm. *B:* example noise-evoked response from simultaneously recorded topographically aligned pair of neurons. *C:* recovered STA for the example units. The black dashed vertical line indicates the time of the spike. The gray bars indicate the confidence interval on an uncorrelated process. On the right, the VPM STA is plotted with a 2-ms delay on the S1 STA as a gray dashed trace. *D:* representative example thalamic and cortical STAs. *E:* *Top* shows first two principal components (PCs) computed using principal component analysis (PCA) of all recovered STAs for thalamic neurons ($n=30$) and cortical neurons ($n=32$). *Bottom* shows the corresponding percent variance explained by all of the components, with the first two capturing the large majority. *F:* temporally aligned thalamic and cortical principal components. Overlay of temporally shifted thalamic PCs (shift of 2.5 ms, sign of VPM PC1 is inverted) on cortical PCs shown as dashed curves (VPM PC1: black dashed, VPM PC2: gray dashed). a.u., arbitrary units; STA, spike-triggered average; Stim, stimulation; S1, primary somatosensory cortex; VPM, ventral posteromedial.

interspike interval of less than 4 ms with the first spike in the burst preceded by 100 ms of silence (Fig. 2A, see METHODS). Using this classification, we asked if or how the feature selectivity of an individual thalamic unit changes as a function of the spiking mechanism in the whisker pathway.

In the thalamic recordings, tonic and burst spikes were interspersed throughout most of the recordings. For the example thalamic unit presented in Fig. 1C, we computed the spike-triggered average from all spikes (STA), the tonic spike-triggered average from only tonic spikes (tSTA), and the burst spike-triggered average from only spikes that are classified as being part of a burst (bSTA; Fig. 2B). The tSTA

(gray) closely resembles the STA computed from all spikes (black) while the bSTA (red) is significantly degraded as evidenced by the flat shape of the filter. To compare the difference between burst and tonic feature selectivity across thalamic units, we quantified the signal-to-noise ratio of the STA (STA_{SNR} , see METHODS). Across all thalamic units, the STA_{SNR} was higher for tonic spikes ($tSTA_{SNR}$) than for burst spikes ($bSTA_{SNR}$; Fig. 2C). We also performed spike count controls for tSTA (Fig. 2C; black dots, discussed further in *Temporal Precision of Thalamic Firing Modes*). Note that again we calculated the STC under these conditions and found the same result that the STC_{SNR} was higher for tonic spikes than for burst spikes ($P=2e-4$, data not shown), and

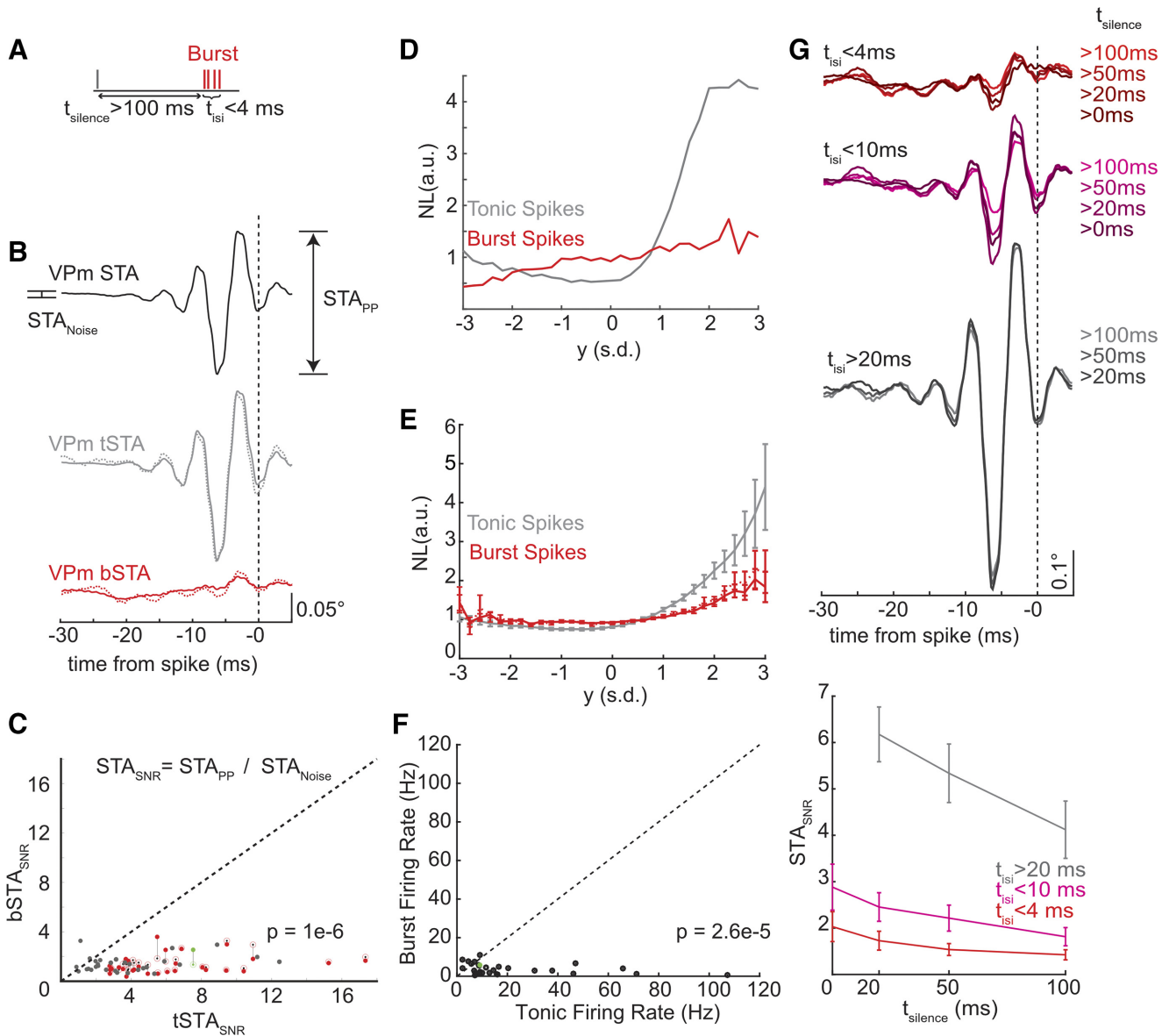


Figure 2. Spike-triggered analysis of burst and tonic spikes in thalamic neurons. **A:** burst definition. **B:** STA from thalamic unit presented in Fig. 1 estimated from all spikes (black solid line, $n = 44,105$ spikes), tonic spikes (tSTA; gray solid line, $n = 36,558$ spikes), a subsample of tonic spikes (tSTA; dashed line, $n = 2,363$ of $36,558$ spikes), all burst spikes (bSTA; red solid line, $n = 7,547$ spikes), and the first spike in the burst (bSTA; red dashed line, $n = 2,363$ spikes). **C:** STA_{SNR} across recorded population ($n = 30$ units). Red dots depict the STA_{SNR} for all bSTA computed from all burst spikes while open red circles indicate the STA_{SNR} for bSTA computed from only the first spike in the burst ($P = 1e-6$). The vertical bars are used to connect the dots coming from the same unit for visualization of the effect of isolating the first spike in the burst. Gray dots indicate the tSTA_{SNR} when computed from a subset of tonic spikes matching the number of burst spikes. Green dot indicates the points for the example unit in **B**. **D:** example unit tonic and burst spike nonlinearity. The nonlinearity (NL) is estimated as the ratio of the $p(y|spike)/p(y)$ and is presented in arbitrary units (a.u.). NL is binned according to the standard deviation (s.d.) of the filtered stimulus (y) distribution. **E:** average nonlinearity across all units. **F:** burst and tonic firing rate [$p(spike)$] across recorded population ($n = 30$ units, $P = 2.6e-5$). Green dot denotes example unit in **B**. **G:** spike-triggered average using different spike classifications (see METHODS). *Top:* example unit STA given different spike classifications ($t_{isi} < 4$ ms: four shades of red, $t_{isi} < 10$ ms: four shades of pink, $t_{isi} > 20$ ms: four shades of gray). *Bottom:* average STA_{SNR} across all recovered thalamic units for each spike classification ($n = 30$ units, $t_{isi} < 4$ ms: red, $t_{isi} < 10$ ms: pink, $t_{isi} > 20$ ms: gray). a.u., arbitrary units; bSTA, burst spike-triggered average; bSTA_{SNR}, signal-to-noise ratio of the burst spike-triggered average; $p(spike)$, firing rate; $p(spike|y)$, probability of eliciting a spike given a filtered stimulus value, y ; $p(y)$, probability of the filtered stimulus; STA, spike-triggered average; STA_{noise}, STA variability amplitude; STA_{PP}, STA peak-to-peak amplitude; STA_{SNR}, signal-to-noise ratio of the spike-triggered average; t_{isi} , two or more spikes with an interspike interval; $t_{silence}$, period with no spiking before the first spike in the burst of at least 100 ms; tSTA, tonic spike-triggered average; tSTA_{SNR}, signal-to-noise ratio of the tonic spike-triggered average; VPm, ventral posteromedial.

that there was not a fundamental shift in representation between tonic and burst spiking.

If the timing of spikes within a burst is not repeatable and structured, the presence of these additional spikes will serve

to destroy the temporal structure in the feature selectivity as revealed by the spike triggered analysis. When the bSTA was computed from only the first spike in each burst (Fig. 2B, red-dashed line), there was still no significant feature

selectivity for this example unit. This can also be visualized across units in the STA_{SNR} where the $bSTA_{SNR}$ is plotted when computed from all burst spikes (black dot) and when computed from the first spike in each burst (red circle, Fig. 2C). Therefore, including all spikes in a burst (or not) does not strongly impact the ability to estimate the feature selectivity from the STA.

Given the estimated feature selectivity, we can compute the static nonlinearity, or the input-output function, which provides a mapping between this filtered stimulus (y), which is the sensory stimulus convolved with the STA of a given unit, and the spiking response of the neuron [$p(\text{spike}|y)$; probability of eliciting a spike given a filtered stimulus value, y ; see METHODS]. The slope of the nonlinearity reflects the degree to which the neuron is “tuned” to the stimulus feature represented by the STA, as defined by the filtered stimulus. When the feature selectivity closely matches the sensory stimulus, the filtered stimulus (y) will be maximized. If the neuron is strongly tuned to the STA, the probability of spiking, $p(\text{spike}|y)$, will be selective for higher filtered stimulus (y) values. If the neuron is not strongly tuned to the STA, then the probability of spiking, $p(\text{spike}|y)$ will be invariant to the filtered stimulus such that the slope of the nonlinearity is flat. Therefore, a steep slope indicates that sensory stimuli that closely resemble the STA of the neuron will drive the neuron to fire whereas a shallow slope indicates that the similarity between the sensory stimulus and the STA is not a strong predictor of the spiking response. Here, we used the tSTA as the filter for all spiking conditions when estimating the nonlinearity. The probability of the filtered stimulus $p(y)$ remains unchanged when the filter is held constant. Therefore, any difference in the nonlinearity is then only due to differences in the probability of the filtered stimulus given that a spike occurred [$p(y|\text{spike})$]. In this example unit, we found that the tonic spikes were well tuned to the STA, as evidenced by the steep slope of the nonlinearity, whereas the burst spikes were not well tuned to the STA, as evidenced by the relatively flat nonlinearity (Fig. 2D). Here, the nonlinearity (NL) is defined as the $p(y|\text{spike})/p(y)$. This trend was consistent across units where the burst spikes showed reduced tuning to the tSTA as compared with tonic spikes as assessed by the slope of the spiking nonlinearity (Fig. 2E). Here, we have separated the difference in the slope of the nonlinearity from the difference in the prevalence of burst and tonic spikes [$p(\text{spike})$ or firing rate], which is markedly higher for tonic spikes than for burst spikes (Fig. 2F).

The classification of spikes belonging to a T-type calcium channel burst is based on criteria on the interspike intervals (see METHODS). The measures here could thus be sensitive to the specific criteria imposed. We therefore tested alternative burst spike classifications and quantified the implication for the STA. Thus far, we classified a burst spike as being two or more spikes with an interspike interval of less than 4 ms ($t_{\text{isi}} < 4$ ms) and a period with no spiking before the first spike in the burst of at least 100 ms ($t_{\text{silence}} > 100$ ms). However, if we relax this definition to allow the silence window to shorten ($t_{\text{silence}} > 100$ ms) while maintaining the strict interspike interval ($t_{\text{isi}} < 4$ ms), the STA_{SNR} remains largely unchanged (Fig. 2G, top: example unit in red scale, bottom: summary data in red). If we further relax the burst condition to allow the interspike interval to be up to 10 ms

($t_{\text{isi}} < 10$ ms), the STA_{SNR} is larger but does not achieve the levels seen for tonic spikes (Fig. 2G, top: example unit in pink scale, bottom: summary data in pink). If we now restrict the tonic spikes to only include spikes that have a minimum of a 20-ms interspike interval with the next spike ($t_{\text{isi}} > 20$ ms), the STA_{SNR} is maximized (Fig. 2G, top: example unit in grayscale, bottom: summary data in gray). This suggests that any tonic spiking incorrectly classified as part of a burst would serve to increase the amplitude, and thus the SNR, of the burst-triggered average, but the conservative definition of a burst pattern that we have used here likely minimizes this effect. The opposite is also the case such that burst spikes that are misclassified as tonic would reduce the amplitude of the tSTA. Interestingly, across spiking classifications, increased periods of silence before the spike (t_{silence}) tended to lead to decreased STA_{SNR} , as shown for the example at the top of Fig. 2G. Although the relationship was somewhat variable for this particular example, on average across the larger data set, there was a monotonic relationship between t_{silence} and STA_{SNR} , regardless of the burst/tonic classification (Fig. 2G, bottom), presumably due to more strictly excluding tonic spiking from the analysis. Therefore, our data suggests a reduction in stimulus selectivity for burst spiking perhaps not due to a true loss of feature selectivity, but instead due to changes in temporal precision relative to the timescale of the stimulus features to which this analytic framework is particularly sensitive.

Optogenetic Manipulation of Thalamic State

The previous analysis was conducted by presenting sensory white-noise stimuli and parsing measured thalamic spiking activity into tonic and burst classes, while these classes of spiking were intermingled throughout the recordings. However, the thalamus was in tonic firing mode, with relatively low burst firing rates (Fig. 2F). Additionally, when bursts do occur intermittently, presumably this is due to a local transient fluctuation in thalamic membrane potential, rather than a sustained change in membrane potential that would be reflective of thalamic “state.” Here, we used optogenetic hyperpolarization of the thalamic neurons not to silence the thalamic neurons, but instead to shift the thalamus into a burst firing mode during sensory white-noise stimulation (Fig. 3A). Using this optogenetic manipulation, we asked whether the optogenetically manipulated firing mode (baseline and hyperpolarized conditions) of the thalamus impacts encoding as measured through the STA analysis used previously.

Here, we transfected excitatory thalamic neurons with a hyperpolarizing opsin. Successful targeting of opsin expression to VPM was confirmed functionally by first classifying neurons as putatively VPM neurons (see METHODS) and then as light responsive by looking at the light offset rebound response. Opsin expression was confirmed histologically by the expression location within the thalamus as well as the expression of the axon terminals within S1 L4 barrels (Fig. 3A). We recorded the thalamic response to sensory white noise with and without the presence of an optogenetic light stimulus (hyperpolarized and baseline conditions, respectively). Surprisingly, we found no significant change in the thalamic firing rate between hyperpolarized and baseline

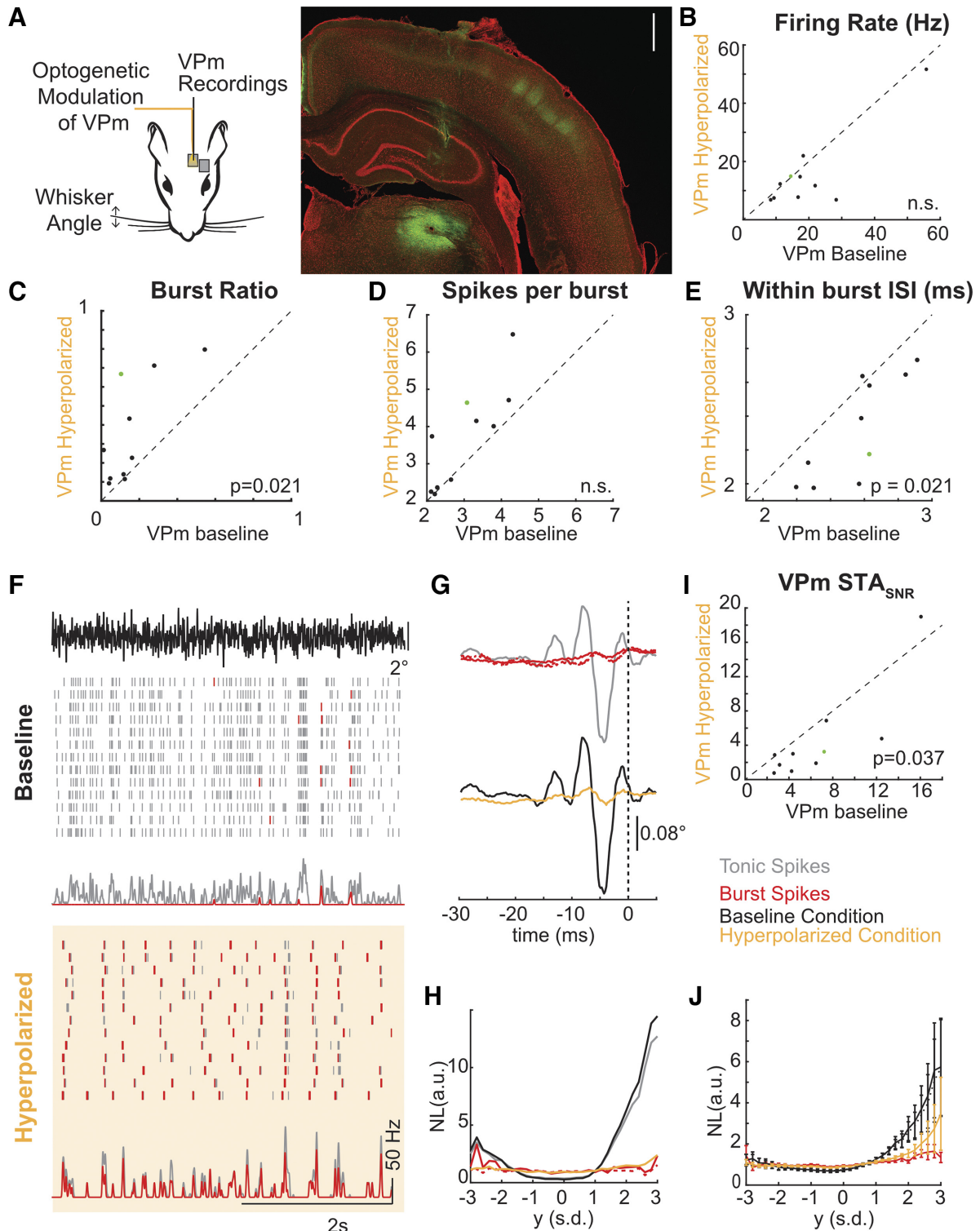


Figure 3. Optogenetic manipulation of thalamic state. **A:** experimental paradigm. Scale bar: 1 mm. YFP signal (green) shows injection site in thalamus and axonal projections in cortex. **B:** baseline and hyperpolarized firing rate [$p(\text{spike})$] across recorded population ($n=10$ units. $P > 0.05$). In all subpanels, the example unit in panels **F–H** is indicated by a green dot. **C:** characterization of the burst ratio ($P = 0.021$). **D:** the spikes per burst ($P > 0.05$). **E:** the within burst ISI ($P = 0.021$) during baseline and hyperpolarized conditions across the population of thalamic units ($n=10$ units). **F:** example thalamic response to frozen white-noise segments without (baseline) and with (hyperpolarized) optogenetic manipulation. Tick marks in raster plot are pseudocolored to demonstrate classification as burst (red tick) or tonic (gray tick) spikes. **G:** spike-triggered average computed as a function of spike classification (burst/red, first spike in burst/red dashed, tonic/gray) or optogenetic condition (baseline/black, hyperpolarized/yellow). **H:** example unit tonic/burst and baseline/hyperpolarized spike nonlinearity. **I:** STA_{SNR} across recorded population ($n=10$ units). **J:** average nonlinearity across all units ($n=10$ units). a.u., arbitrary units; ISI, interspike interval; NL, nonlinearity; STA, spike-triggered average; STA_{SNR}, signal-to-noise ratio of the spike-triggered average; VPM, ventral posteromedial; y , filtered stimulus value; YFP, yellow fluorescent protein.

conditions (Fig. 3B), but the firing mode of the thalamus did shift toward burst firing (baseline burst ratio = 0.16 ± 0.15 , hyperpolarized burst ratio = 0.36 ± 0.27 , $n = 10$ units, Fig. 3C). Because the mean firing rate in VPM in response to sensory white noise was not significantly different between the baseline and hyperpolarized conditions, this is reflecting a “replacement” of tonic firing with burst firing. Bursts in the hyperpolarized condition showed a similar number of spikes per burst (Fig. 3D) with a shorter interspike interval within a burst (Fig. 3E). For a small subset of neurons, we collected responses to frozen white noise. For an example unit, we have plotted the spiking response to a frozen white-noise segment without optogenetic manipulation (Fig. 3F, baseline condition) and with optogenetic manipulation (Fig. 3F, hyperpolarized condition). We have pseudocolored the tonic spikes gray and the burst spikes red to qualitatively visualize the thalamic firing mode (Fig. 3F). In the baseline condition, the response is primarily tonic as evidenced by the gray raster plots (Fig. 3F, baseline, BR = 0.10). In the hyperpolarized condition (optogenetically manipulated), the firing mode is biased toward a burst encoding scheme, as evidenced by the prevalence of red burst spikes (Fig. 3F, hyperpolarized, BR = 0.67). The STA analysis was conducted in two different ways. First, as in Fig. 2, the analysis was conducted from the classified tonic and burst spikes. The tonic STA showed pronounced feature selectivity for this unit while the burst STA did not (Fig. 3G red/gray), consistent with the earlier findings reflective of the loss in timing precision for the first spike of a burst (Fig. 2). Second, the STA analysis was repeated for each condition, where the baseline STA was computed for all spikes in the baseline condition and the hyperpolarized STA was computed for all spikes in the hyperpolarized condition. The baseline STA has prominent feature selectivity while the hyperpolarized condition is much smaller in amplitude (Fig. 3G, yellow/black). Qualitatively, we can see that the STA from the hyperpolarized condition reflected the STA obtained from the burst spiking in the previous analysis. Again, a subsequent analysis of the STC revealed representations that were redundant with the spike-triggered average, and no apparent shift in feature selectivity between the tonic and burst firing modes.

The similarity between the analyses based on burst spiking and in the hyperpolarized condition can also be seen in this example nonlinearity where the burst and hyperpolarized nonlinearities are effectively flat while the tonic spikes and baseline condition show obvious tuning as evidenced with steep slopes (Fig. 3H). Across units, we found an overall reduction in the STA_{SNR} for the hyperpolarized condition relative to the baseline condition (Fig. 3I, $P = 0.037$). We also found that the tuning (i.e., selectivity to the particular sensory feature represented by the STA) was lower for the hyperpolarized condition relative to the baseline condition as reflected in the overall gain/slope of the nonlinearity (Fig. 3J). Importantly, the baseline and hyperpolarized conditions both contain burst and tonic spikes to varying degrees. For this analysis, we have optogenetically altered the spiking probabilities such that the baseline condition has more tonic spikes and the hyperpolarized condition has more burst spikes (Fig. 3C) while maintaining similar numbers of spikes (Fig. 3B). The similarities between the STA and the NL properties when the analysis was based on burst spikes versus all

spikes in the hyperpolarized condition, as well as when the analysis was based on tonic spikes versus all spikes in the baseline condition, suggest that there was no discernable difference for the estimation of feature selectivity when assessed based on the state of the thalamus (hyperpolarized/baseline) versus the spike type classification (burst/tonic). Thus, the properties of the burst spiking are similar when the thalamus is artificially induced into a burst mode through optogenetic hyperpolarization, as compared with the burst spiking that occurs intermittently in the baseline case due to local transient fluctuations in thalamic membrane potential.

Temporal Precision of Thalamic Firing Modes

Given the difference between the recovered estimates of burst/hyperpolarized and tonic/baseline feature selectivity and the implications for timing precision in the thalamocortical circuit, we implemented a series of computational controls to identify any potential shortcomings of the methodologies that could underlie these results.

The first issue we considered was the overall difference in spike rates. Spike-triggered analyses require a large number of spikes to effectively estimate the underlying selectivity. The proportion of spikes classified as bursts was lower than the spikes classified as tonic (Fig. 2F) as quantified by the burst and tonic firing rate. Therefore, it was possible that we could not recover an STA for the burst spiking due to the reduced number of burst spikes relative to tonic spikes. In an example unit, we computed the tSTA using only a subset of the spikes ($n = 2,363$ of 36,558 spikes corresponding to $n = 2,363$ bursts with $n = 7,547$ burst spikes) and found that the linear filter was essentially identical to the tSTA (Fig. 2B, gray dashed line). We computed this for all thalamic units and again found that the burst-count matched tSTA was also significantly larger than the bSTA (Fig. 2C; black dots). Furthermore, there was no statistically significant difference in the firing rate between the baseline and hyperpolarized optogenetic conditions (Fig. 3B), but still the difference in the STA persisted. This suggests that simple spike counts alone were insufficient to explain the difference in the tonic/baseline STA and the burst/hyperpolarized STA.

The second issue we considered was the inherent assumption that the feature selectivity for each unit could be recovered as the STA. It was possible that the burst STA was not recoverable because the burst firing mode was better estimated by a symmetric nonlinearity and therefore the filter could only be recovered using spike triggered covariance (STC) techniques. The STC approach has been previously implemented in the vibrissa pathway (19, 20, 36), revealing potential feature selectivity not captured with STA and was therefore important to consider here. We therefore computed the STC for all recorded thalamic units and compared this for each spiking condition. Although the data set was more limited because the number of units with a significant STC filter was lower than those with a significant STA filter ($n = 13$ units with STC filter compared with $n = 30$ units with STA filter), the same trends regarding the reduction in the amplitude of the filter (STC_{SNR}) and the slope of the symmetric nonlinearity persisted (as described in RESULTS). Therefore, this suggests that the method of extracting the feature selectivity

(STA compared with STC) was insufficient to explain the inability to estimate the feature selectivity in the hyperpolarized/burst spiking conditions. However, it is also possible that the feature selectivity for a given neuron shifts to a higher-order space as firing modes transition from tonic to burst firing. If the burst firing could be associated with higher-order structure in the sensory stimulus, it may only be revealed using STC analysis. We thus conducted a STC analysis of the recorded neurons. First, we found that the tonic STA_{SNR} was significantly larger than the burst STC_{SNR} ($P = 3e-6$), suggesting that the feature selectivity did not simply shift from the first-order estimate of the STA to higher order representations captured by the STC. Then we assessed the probability that a unit with a significant filter, as assessed using STA, also showed a significant filter, as assessed using STC. We found that all 13 units with significant STC filters also showed significant STA filters. This emphasizes the complexity of the stimulus representation but further underscores that the stimulus representation did not simply shift from tonic to burst firing. Therefore, this analysis revealed that in general the high-order structure captured by STC was insignificant compared with the first-order structure revealed by STA, and that when there was a loss of structure in the STA in the burst mode of firing, no new higher-order feature selectivity emerged through the STC analysis.

The third assumption made throughout the analysis was that burst spikes are actually driven by sensory stimuli such that there is a recoverable burst spike feature selectivity. The alternative explanation would be that burst spikes are not feature selective and instead occur randomly due to intrinsic or other nonsensory processes. As can be seen in Fig. 3F, the qualitative assessment of temporally aligned bursts in response to the frozen white-noise segment suggests that the bursts are driven by the sensory stimulus in a repeatable way. Although this is a qualitative observation, this suggests that the bursts are not randomly generated or due entirely to a nonstimulus-related phenomenon.

From these controls, we propose that the difference in the spike-triggered encoding properties could not be attributed to differences in the overall spike rates, the temporal properties of the spikes within the burst, or the mechanism of filter estimation. Instead, we propose that the burst spikes are driven by the sensory stimulus and have an underlying feature selectivity, but that burst spiking has reduced temporal precision relative to tonic spiking as reflected in the STA analysis.

Recovering feature selectivity from spike-triggered analysis relies on precise temporal spiking relative to the sensory stimulus. The STA analysis relies on long sequences of unique (unfrozen) white noise stimulus sequences, and thus many of the recorded units were not presented with multiple repetitions of frozen white noise sequences, precluding a direct assessment of timing variability (see METHODS). However, the effects of timing variability can be assessed through simulation. To simulate degradation of the spike timing precision, we added independent samples of normally distributed temporal jitter of varying amplitudes (standard deviation of the jitter distribution) to each tonic spike for an example unit and computed the STA (Fig. 4A). Across units, we quantified the degradation of the STA as the jittered- STA_{SNR} normalized by the $tSTA_{SNR}$ (0-ms jitter). The

jittered- STA_{SNR} (black) is within the band expected for the $bSTA_{SNR}$ with the addition of 4 ms of jitter to the spike times (red shaded, Fig. 4A, right). We propose that the effects of temporal jitter are particularly evident for whisker selectivity, presumably due to the short temporal duration of the filters (~ 10 – 15 ms in duration, Fig. 1F).

Given the marked effects of jitter on the ability to recover the STA, we investigated the variability in the spike timing relative to the noise stimulus (Fig. 4B). For this example unit, we have identified a segment in the noise stimulus that closely resembles the tonic STA for this unit and elicits a reliable spiking response (Fig. 4B, top; stimulus—black, tSTA—gray dashed). The vertical dashed line indicates the spike time for the spike triggered average (t_0). If there was no variability in the neural spiking, the raster plots would all be perfectly aligned to t_0 because the similarity between the stimulus and the STA would predict a spiking response at that time point. However, the timing of evoked neural responses is always variable to some extent and this can be visualized for this example response segment as the temporal variability of the spike times surrounding this stimulus feature in the noise stimulus (Fig. 4B). For this example snapshot, it is also apparent that the burst spikes in the hyperpolarized condition show greater temporal variability than the tonic spikes in the baseline condition.

To quantify this jitter across all spikes, we developed a τ_{jitter} metric that determines the time lag of the peak correlation between the STA and the stimulus segment [$s(t_i)$] surrounding each spike (Fig. 4C). Intuitively, this is a correlative method to identify the time lag between when we predict a spike is most likely to occur based on the STA and the stimulus (peak correlation) and when the spike actually occurred. For this analysis, we treated the tSTA as the true feature selectivity of the neuron across all spiking conditions because we could not recover a reliable estimate of the bSTA.

We computed τ_{jitter} for each spike and plotted τ_{jitter} distributions for tonic spikes, burst spikes, hyperpolarized condition, and baseline condition. If a neuron was infinitely precise such that when the stimulus matched the spike-triggered average, the neuron fired a spike without delay, this distribution would be represented by a delta function at τ_{jitter} equals zero. As the variability of the timing increases, the width of this distribution will also increase. For the tonic spiking and baseline condition, we found a clear peak in τ_{jitter} values at τ_{jitter} equals zero (Fig. 4C, gray, black). For the burst spiking and hyperpolarized condition, we observe little-to-no peak in the τ_{jitter} metric at zero (Fig. 4C, red, yellow). We computed the τ_{jitter} distribution across all thalamic units and found that the tonic spiking and baseline condition had higher peaks at τ_{jitter} equals zero than the burst spiking and hyperpolarized condition (Fig. 4D). We quantified this statistically by computing a precision metric (Fig. 4C) that computes the proportion of spikes within ± 1 ms of τ_{jitter} equals zero (Fig. 4E). The tonic spiking and baseline condition were more precise than burst spiking and hyperpolarized condition.

These data suggest that tonic spiking showed greater temporal precision in response to the sensory white-noise than burst spiking and that this could underlie the difference in the recoverability of the feature selectivity in the thalamus between firing modes. It is well established that the timing

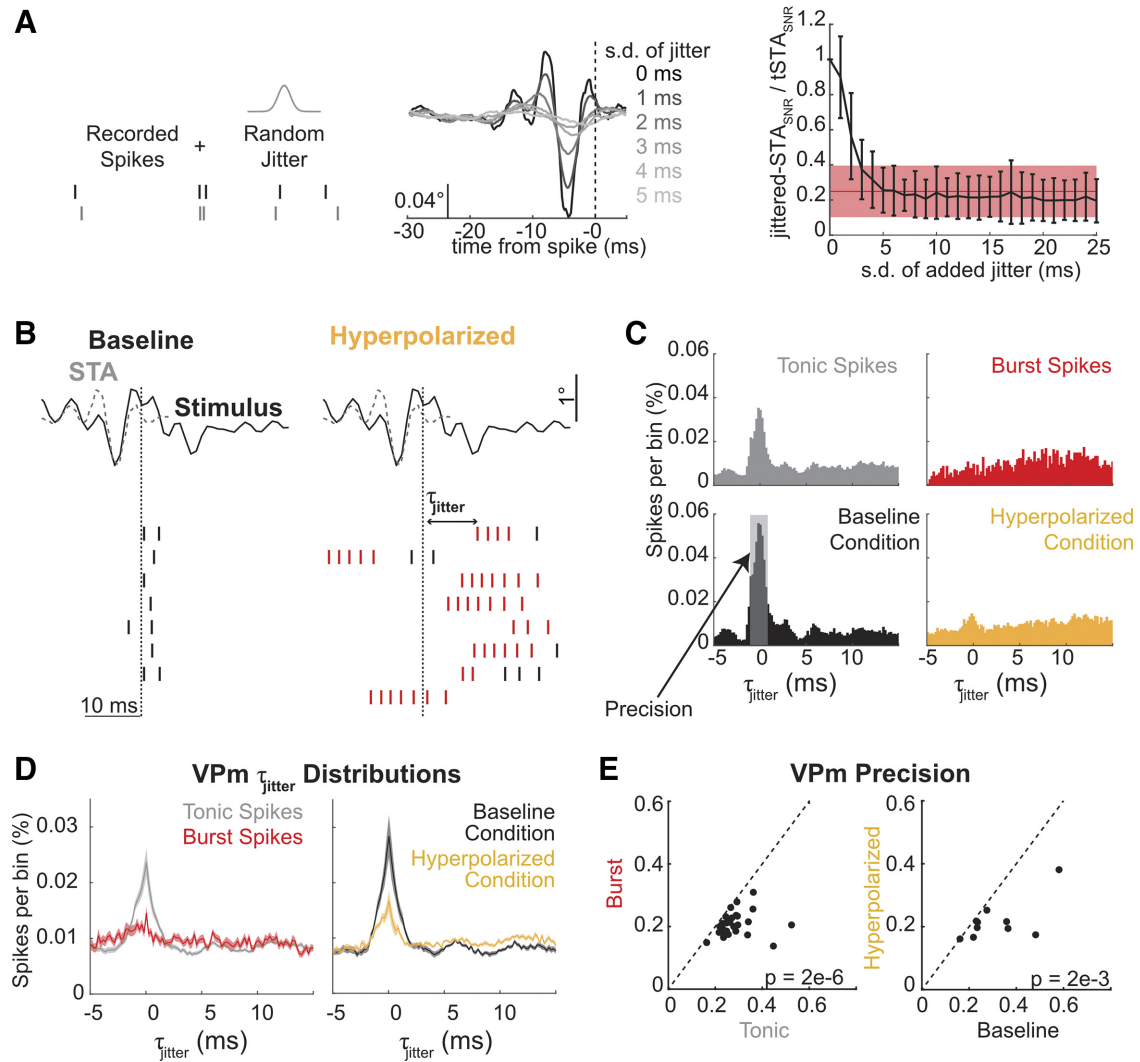


Figure 4. Thalamocortical timing variability in the response to the sensory white noise. *A*: effect of increased jitter on thalamic STA (schematic: *left*, example: *center*). Across units ($n = 30$), the normalized amplitude of the jittered STA (jittered STA_{SNR}/tSTA_{SNR}) was plotted across jitter intensities (black, *right*). The normalized amplitude of the burst STA (bSTA_{SNR}/tSTA_{SNR}) is shown in red (mean \pm SD). *B*: in this example, the same stimulus (black; scale bar: 0.1°) was presented with and without optogenetic hyperpolarization [data from example unit presented in Fig. 3 with associated STA (gray dotted line)]. *C*: example unit τ_{jitter} distributions for burst spikes ($n = 2,107$ spikes), tonic spikes ($n = 23,023$ spikes), baseline condition ($n = 11,361$ spikes), and hyperpolarized condition ($n = 11,662$ spikes). *D*: average τ_{jitter} distributions for burst/tonic spikes ($n = 30$ units) and baseline/hyperpolarized condition ($n = 10$ units; mean \pm SE). *E*: precision for burst/tonic spikes ($n = 30$ units, $P = 1e-6$) and baseline/hyperpolarized condition ($n = 10$ units; mean \pm SE, $P = 1e-3$). bSTA_{SNR}, signal-to-noise ratio of the burst spike-triggered average; STA, spike-triggered average; tSTA_{SNR}, signal-to-noise ratio of the tonic spike-triggered average; VPM, ventral posteromedial.

of sensory inputs is particularly important in the thalamocortical circuit such that changes in thalamic spike timing could have large impacts on the downstream representation of sensory information in the cortex. Next, we investigated how these changes in temporal precision in optogenetically modulated thalamic states impact cortical encoding properties.

Optogenetic Modulation of Thalamic Firing Modes Directly Impacts Cortical Timing Precision

Cortical neurons that receive direct thalamic input are integrating information over a population of thalamocortical neurons that can be exhibiting different firing characteristics. This makes it difficult to determine the impact of

a single burst from a single neuron on information representation in the pathway. Instead, we used the optogenetic manipulation of thalamic state as presented in Fig. 3 to bias the activity of the thalamic population toward burst firing (hyperpolarized condition) while recording the cortical activity extracellularly to quantify the effect of bursting downstream (Fig. 5A).

For an example unit, we have plotted the cortical STA in the baseline and hyperpolarized VPM conditions (Fig. 5B). Here, the amplitude of the cortical STA was smaller when the thalamus is hyperpolarized compared with when it is not (Fig. 5B). This cortical unit also shows a reduced slope of the nonlinearity when the thalamus was hyperpolarized (Fig. 5C), and thus a decrease in tuning to the stimulus feature represented by the STA. Across the population of recorded

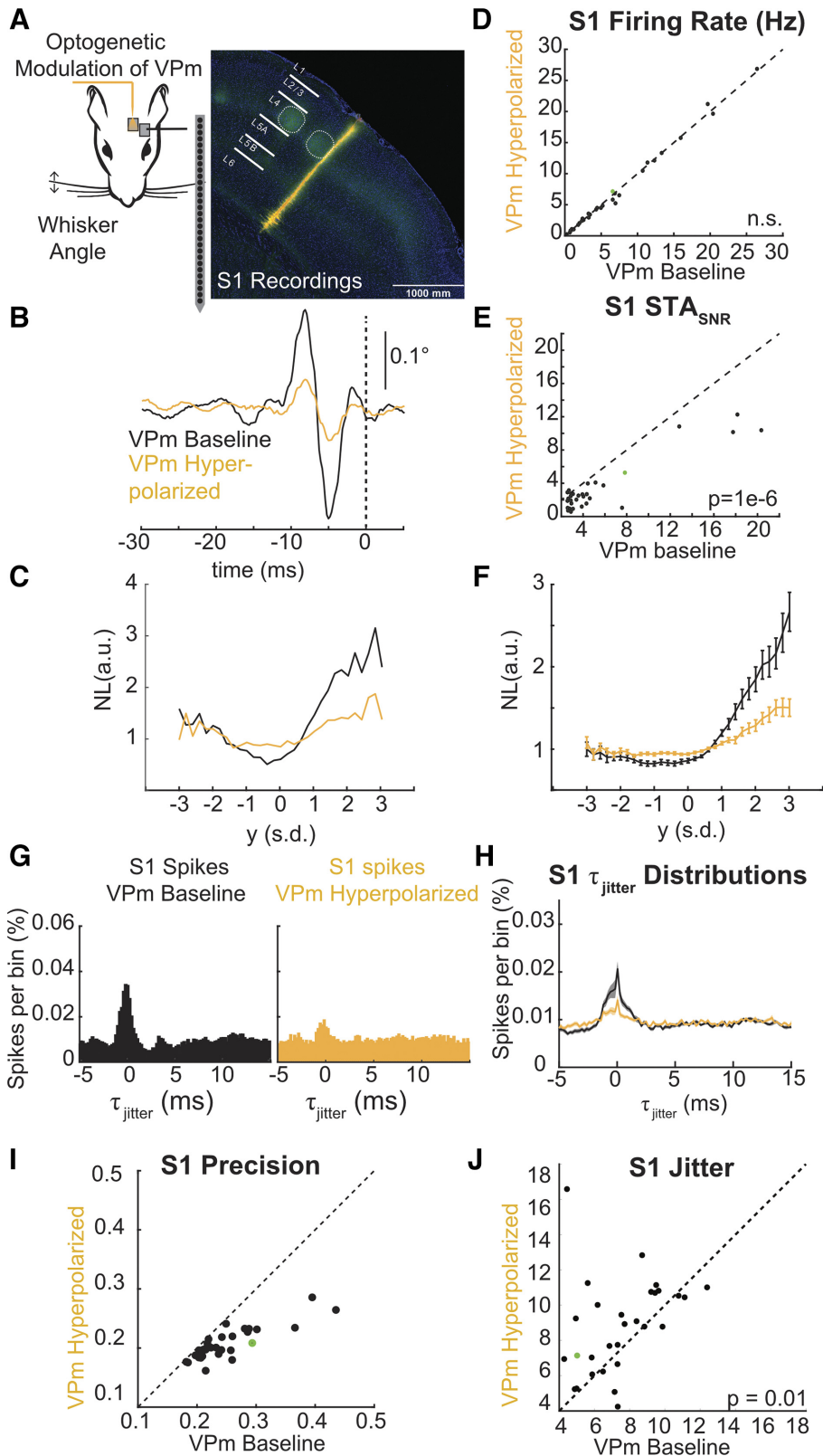


Figure 5. Optogenetic modulation of thalamic firing modes directly impacts cortical representation of sensory information. **A:** experimental paradigm. Scale bar: 1 mm. YFP signal (green) shows axonal projections into cortex. A fluorescent dye (Dil) was used on the probe to confirm recording location. **B:** example STA for a cortical unit recorded during optogenetic manipulation of the thalamus (black: baseline thalamic condition, yellow: hyperpolarized thalamic condition). **C:** example cortical nonlinearity as a function of thalamic state. **D:** cortical firing rate during thalamic manipulation ($n=32$ units, $P=0.31$). **E:** STA_{SNR} across cortical units ($n=32$ units; $P=1e-6$). **F:** spiking nonlinearity across cortical units during thalamic manipulation ($n=32$ units). **G:** example cortical unit τ_{jitter} distributions for baseline ($n=12,862$ spikes) and hyperpolarized ($n=11,848$ spikes) thalamic conditions. **H:** average τ_{jitter} distributions for baseline/hyperpolarized thalamic condition ($n=32$ units, mean \pm SE). **I:** precision for cortical spikes during baseline/hyperpolarized thalamic condition ($n=32$ units, $P=8e-6$). **J:** trial-to-trial jitter for cortical spikes in response to frozen white-noise segments during baseline/hyperpolarized thalamic conditions ($n=32$ units, $P=0.01$). a.u., arbitrary units; NL, nonlinearity; n.s., not significant; STA, spike-triggered average; STA_{SNR}, signal-to-noise ratio of the spike-triggered average; S1, primary somatosensory cortex; VPm, ventral posteromedial; y, filtered stimulus value; YFP, yellow fluorescent protein.

cortical neurons, the same effect seen in this example neuron of a reduced STA_{SNR} when the VPm was hyperpolarized compared with when it was not (Fig. 5E) and a reduction in the slope of the nonlinearity was present (Fig. 5F). These

findings mirror what was seen for thalamic neurons when comparing the baseline and the optogenetically manipulated conditions demonstrating that the changes in thalamic encoding properties are propagated to cortex. Note that we

again conducted the STC analysis with the S1 neurons and found the same reduction in STC_{SNR} when the VPM was hyperpolarized compared with when it was not ($P=9e-5$), suggesting that the loss of feature selectivity in S1 with thalamic hyperpolarization was not just due to the transfer of feature selectivity to higher-order characteristics.

Interestingly, there was no significant difference in the stimulus-evoked firing rate in the cortex in the baseline and thalamic hyperpolarized conditions (Fig. 5D). This suggests that it was not overall spike counts influencing the cortical feature selectivity. Instead, we propose the temporal jitter in the thalamic spiking patterns propagated to cortex. We investigated the temporal precision of the cortical spiking in response to the sensory white noise using the same methodology employed for the thalamus. As we saw for the thalamus, the cortical spikes from this example unit also showed greater temporal precision in response to white-noise whisker stimulation in the baseline VPM condition compared with the hyperpolarized VPM condition (Fig. 5G) as evidenced by the peak in the τ_{jitter} distribution around τ_{jitter} equals zero. This effect was consistent across the population of recorded cortical units (Fig. 5H) and showed significant differences in the precision of the cortical firing (Fig. 5I). We further analyzed the trial-to-trial jitter from the cortical responses to frozen white noise segments. We identified events as peaks in the peristimulus time histogram and aligned these events to generate an event aligned histogram. A Gaussian function was fit to this histogram and the standard deviation was defined as the trial-to-trial jitter (see METHODS). Confirming the jitter metric defined for thalamic units, the trial-to-trial jitter metric also showed an increase in the hyperpolarized thalamic condition relative to the baseline thalamic condition (Fig. 5J). This suggests that the temporal jitter present in the thalamus is transmitted to the cortex.

DISCUSSION

Although there have been extensive investigations into the cortical state-dependent processing of the thalamocortical circuit (45), we know surprisingly little about how information is processed in a thalamic state-dependent manner. Here, using a combination of optogenetic manipulation and electrophysiological recording techniques, we have performed a series of experiments modulating the state of the thalamus (through constant optogenetic hyperpolarization) and quantified the effects on encoding in the thalamocortical circuit. Using this technique, we have coarse control of the firing mode in thalamus without altering the processing occurring from the whisker to thalamus, enabling us to decouple the changes in thalamic firing mode on thalamocortical processing from changes occurring in subthalamic processing. We found that thalamic burst firing, during both baseline activity and in optogenetically induced burst mode, was associated with a loss of apparent feature selectivity on precise timescales revealed through spike-triggered analysis, consistent with an increase in burst spike timing variability (loss of timing precision) relative to tonic spike timing. Corresponding recordings from barrel cortex during optogenetically induced thalamic burst mode demonstrated a loss in the temporal precision of the cortical spiking that also led

to a degradation of the recovered feature selectivity. This suggests that, although both thalamus and cortex remain well driven by sensory input during optogenetically induced thalamic burst mode, bursts in the whisker pathway are less precise than tonic spikes during ongoing weak sensory stimulation and that this loss of temporal precision is propagated to cortex, which could have implications for the integration of complex patterns of sensory inputs.

In the visual pathway, distinct sensory selectivity has been identified for burst versus tonic firing (9–13). Although not explicitly forcing the thalamus into a burst mode where bursting is prevalent, as we have done here, these studies found that the burst response is reliably elicited across trials in response to sensory stimulation (11, 13, 14) and the feature selectivity of the bursts is characterized by a prolonged inhibitory stimulus before the depolarizing input that occurs immediately before the spike onset. Furthermore, bursts elicited in response to visual stimulation have been found to be temporally precise on the order of a few milliseconds (9) and alterations in the amount of bursting from a neuron can change its transfer function (46). Studies of the retinogeniculate pathway have also shown that the thalamic burst mode is more likely to elicit a response to incoming retinal spiking inputs (47, 48). Collectively, these earlier studies demonstrated that burst spikes convey relevant sensory information, as quantified through temporal or spatial receptive field mapping, that can be distinct from the tonic spikes (11, 12, 49).

The findings presented here seem counterintuitive relative to some of the findings in the visual pathway and thus deserve further discussion. One critical difference between the visual and the somatosensory pathway is the characteristics of the natural stimulus space. Bursting responses are robust in the representation of natural scenes in the visual pathway (11). Although white-noise stimulation used here provides an unbiased sampling of the stimulus space that enabled estimation of the feature selectivity, it was also a relatively weak stimulus and did not contain the strong transients present in either the binary white noise or the natural scenes previously utilized to probe the visual pathway. Providing more naturalistic stimulation both temporally, with the strong transients associated with stick-slip whisker motions (50), and spatially using multiwhisker coordinated movements (19, 21) could drive different patterns of bursting activity from what is elicited by relatively weak sensory white noise.

Beyond the stimulus selectivity and characteristics, there are also known anatomical differences between the visual and somatosensory thalamus that would directly affect the local inhibition required to elicit a bursting state. Although the rodent whisker thalamus receives its primary inhibition from the thalamic reticular nucleus (TRN) (51), the rodent visual thalamus [lateral geniculate nucleus (LGN)] also has local interneurons that receive direct synaptic drive from the retina. This enables local feedforward and feedback inhibition within the LGN to shape the feature selectivity of the pathway (52, 53). In addition to the complex processing of the visual signals by the retina itself that shape the input to thalamus, the LGN has structured excitation and inhibition in the recovered feature selectivity (ON/OFF) that enables reliable inhibitory stimulation regimes. This might suggest

differences in the temporal precision of the inhibition that directly impacts the precision of burst spiking and could underlie the different burst spike feature selectivity in the visual and somatosensory thalamus.

Although spike-triggered analysis has been widely applied in various pathways, there have been comparatively few studies of this nature in the vibrissa pathway despite the extensive utilization of this model system. In this study, we focused primarily on timing in the thalamocortical circuit, and used the spike-triggered analysis as a vehicle to probe this issue rather than uncovering novel aspects of feature selectivity related to whisker kinematics. Nevertheless, it is important to note the similarities and differences between these studies. Spike-triggered averaging of VPM neurons in a study from Petersen et al. (20) revealed very similar feature selectivity to what we report for VPM in baseline conditions here, with spiking tending to be preceded by a very fast transient, biphasic whisker deflection. Studies in cortex, however, reveal more complex properties. Although the basic feature selectivity that we uncovered for S1 neurons in baseline conditions using STA was very similar to what has been observed in a subset of recorded neurons in other cortical studies (19, 36), further analysis using STC as well as more elaborate whisker stimulation paradigms in these studies identified more complex encoding properties. It should be noted that we restricted analysis to cortical S1 neurons that exhibited significant feature selectivity in the baseline condition with STA, but also observed other cortical neurons that showed significant feature selectivity only using STC, consistent with these previous studies. For these neurons, the filters recovered using STC analysis for tonic spikes were lost when they were computed for burst spikes, as the STC analysis is also reliant on precise spike-timing relative to the sensory stimulus.

It is also theoretically possible that the bursting feature selectivity is not degraded or lost but instead transformed to a type of selectivity that is not captured through the simple characteristics of the spike-triggered averaging. As described above, previous studies have utilized STC analysis to successfully uncover complex feature selectivity in the visual (54) and somatosensory (19, 36) pathways. However, when we extended the analysis here to the spike-triggered covariance (STC), it was not the case that the timing changes were captured through covariance analysis. For both the thalamic VPM and cortical S1 recordings, there was no apparent shift in feature selectivity from first-order structure (STA) to higher-order structure (STC) with a change in thalamic firing mode or state. Units with significant features in the tonic spiking condition did not show significant features in the burst spiking condition, even when assessed using both STA and STC. However, because the feature selectivity of the burst spikes was unrecoverable using spike triggered analysis, we have proposed that the stimulus selectivity is maintained across spiking conditions. This contrasts with what has been shown in other sensory modalities, most notably vision. As with the spike triggered analysis, any burst feature selectivity that is fundamentally different from the tonic feature selectivity cannot be captured in the spike-triggered analysis due to the timing variability of the spiking. This selectivity can only be theoretically identified

through measuring, and compensating for, the increased spike timing jitter, as this framework is inextricably linked to the timing precision with which neurons spike relative to the sensory input.

There are multiple mechanisms that could underlie the reduced temporal precision in the burst firing mode including variability introduced by the slow dynamics of the calcium depolarization, increased variability in the time to reach threshold due to the prolonged hyperpolarization of the baseline polarization, as well as potential changes in the integration properties of the thalamic neurons. Furthermore, these mechanisms could act independently such that the variability across neurons is uncorrelated or these mechanisms could be coordinated in some way to enable correlated variability across the thalamic population. Both coordinated and uncoordinated jitter would have a detrimental effect on the ability to recover the STA because either the spike timing would no longer be locked to the stimulus itself or the input to the cortex would be temporally imprecise. However, coordinated jitter would maintain the information about the stimulus while uncoordinated jitter would degrade the recoverability of the stimulus features with the spike-triggered approach. Future work is needed to investigate the jitter in the burst spiking across the population to determine whether or not the variability in the spike timing is coordinated across thalamic units in this context.

Although thalamic feature selectivity was disrupted for both burst spiking during baseline activity and all spiking during optogenetically induced thalamic burst mode, the utilization of the hyperpolarizing optogenetic scheme was particularly important for capturing the impact of thalamic bursting on the downstream cortical activity in the context of sensory signaling. Cortical layer 4 neurons are thought to be primarily driven through the aggregate synaptic input of 50–100 thalamocortical projections (8). The bursting activity observed during the weak white noise sensory stimulation at baseline is not coordinated across the thalamic population (2). However, the optogenetic manipulation biases the thalamic population towards bursting, enabling the characterization of cortical feature selectivity attributed to modes dominated by either tonic (baseline) or burst (thalamic hyperpolarized) firing. Importantly, we found that the cortical firing rate was remarkably invariant to thalamic hyperpolarization despite the prevalence of thalamic bursting. Further, although we expected to find increased sensitivity of cortical neurons during thalamic hyperpolarization, we found the opposite through the spike-triggered analysis using the weak white noise stimulus here. The effects in S1 were weaker than those seen in thalamus, but we believe this is because the effects are aggregated across the population of thalamic units that have variable opsin expression levels and variable light stimulation due to physical distance from the optic fiber as well as population cortical activity that impacts the variability of sensory encoding (55). This does not, however, necessarily conflict with previous findings that have shown increased thalamocortical synaptic efficacy with thalamic bursts (7) primarily due to the silence period preceding the first spike in the burst (56, 57). Individual projections could have an enhanced effect during bursting, whereas disruption in the timing across thalamic projections could work in the opposite direction. Further,

although viral transfection was targeted to VPm, the opsin expression extended beyond the borders of VPm into neighboring excitatory thalamic nuclei. Although the optrode recordings were specifically targeted to VPm neurons, as identified functionally, it is likely that there was off-target excitation of multiple nuclei, including the posteromedial complex (POm) of the thalamus. Off-target excitation of POm could have compounding effects on the results found here, notably across layers due to the differential projection patterns of VPm and POm thalamocortical axons. Given the uncertainty around feature selectivity in the POm, it would be difficult to predict what impact this would have on the temporal precision. Future work targeting POm state changes would help to elucidate the differential role of POm on detailed sensory encoding in a thalamic state-dependent manner relative to VPm.

These results could be interpreted as consistent with the view that bursts are not representing detailed stimulus information. However, there is evidence that bursts may convey more information than the “all-or-none” presence or absence of a burst through interburst spike timing and the number of spikes per burst (58), suggesting a role of temporally precise burst firing in information representation. Furthermore, thalamic bursting can be temporally precise within and across neurons in response to high intensity whisker stimuli (2). Instead, we propose that the temporal precision of the thalamic firing is a function of both the state of the thalamus and the intensity of the sensory stimulus. It has previously been shown that the temporal precision of thalamic encoding increases with the intensity of the sensory stimulus (2, 59) while here we have shown that the temporal precision of the thalamic firing decreases with sustained hyperpolarization, which would naturally have implications for what signals do and do not get conveyed through the relatively narrow cortical window of integration (60). These two competing factors would enable the burst firing mode to encode high amplitude stimuli in a temporally precise fashion while low amplitude stimuli, such as the sensory white noise presented here, would not be able to overcome the variability present in the burst state, which sets the stage for the selective transmission of elements of the sensory input that may separate “signal” from “noise.”

Although we have primarily considered thalamic state-dependent encoding as a feedforward representation from thalamus to cortex, the highly interconnected thalamocortical circuitry shapes coding properties in both feedforward and feedback manners. Changes in thalamic activity impact cortical activity which then provides feedback to thalamus to further alter activity (4, 61–64). It is possible for the thalamus to influence cortical state and for the cortex to influence thalamic state, but how this plays out during natural behaviors is not yet known and must be decoupled using techniques such as closed-loop control of neural activity (65–67) that enable interactive probing of this complex circuit.

ACKNOWLEDGMENTS

Confocal imaging was performed at the Georgia Tech IBB Imaging Core. We thank Peter Y Borden, Aurélie Pala, Christian

Waiblinger, and Caleb Wright for helpful comments on the data analysis and manuscript.

GRANTS

This work was supported by NIH National Institute of Neurological Disorders and Stroke Grants R01NS085447 and R01NS104928. C. J. Whitmire was supported by the NIH National Research Service Award (NRSA) Predoctoral Fellowship (F31NS089412). Y. J. Liew was supported by the Global Biomedical Engineering Research and Education Fellowship.

DISCLOSURES

No conflicts of interest, financial or otherwise, are declared by the authors.

AUTHOR CONTRIBUTIONS

C.J.W. and G.B.S. conceived and designed research; C.J.W. and Y.J.L. performed experiments; C.J.W. analyzed data; C.J.W. and G.B.S. interpreted results of experiments; C.J.W. prepared figures; C.J.W. and G.B.S. drafted manuscript; C.J.W., Y.J.L., and G.B.S. edited and revised manuscript; C.J.W., Y.J.L., and G.B.S. approved final version of manuscript.

REFERENCES

1. Wolfart J, Debay D, Le Masson G, Destexhe A, Bal T. Synaptic background activity controls spike transfer from thalamus to cortex. *Nat Neurosci* 8: 1760–1767, 2005. doi:10.1038/nm1591.
2. Whitmire CJ, Waiblinger C, Schwarz C, Stanley GB. Information coding through adaptive gating of synchronized thalamic bursting. *Cell Rep* 14: 795–807, 2016. doi:10.1016/j.celrep.2015.12.068.
3. Castro-Alamancos MA. Properties of primary sensory (lemniscal) synapses in the ventrobasal thalamus and the relay of high-frequency sensory inputs. *J Neurophysiol* 87: 946–953, 2002. doi:10.1152/jn.00426.2001.
4. Mease RA, Krieger P, Groh A. Cortical control of adaptation and sensory relay mode in the thalamus. *Proc Natl Acad Sci USA* 111: 6798–6803, 2014. doi:10.1073/pnas.1318665111.
5. Suzuki S, Rogawski MA. T-type calcium channels mediate the transition between tonic and phasic firing in thalamic neurons. *Proc Natl Acad Sci USA* 86: 7228–7232, 1989. doi:10.1073/pnas.86.18.7228.
6. Sherman SM. A wake-up call from the thalamus. *Nat Neurosci* 4: 344–346, 2001. doi:10.1038/85973.
7. Swadlow HA, Gusev AG. The impact of “bursting” thalamic impulses at a neocortical synapse. *Nat Neurosci* 4: 402–408, 2001. doi:10.1038/86054.
8. Bruno RM, Sakmann B. Cortex is driven by weak but synchronously active thalamocortical synapses. *Science* 312: 1622–1627, 2006. doi:10.1126/science.1124593.
9. Alitto HJ, Weyand T, Usrey WM. Distinct properties of stimulus-evoked bursts in the lateral geniculate nucleus. *J Neurosci* 25: 514–523, 2005. doi:10.1523/JNEUROSCI.3369-04.2005.
10. Denning KS, Reinagel P. Visual control of burst priming in the anesthetized lateral geniculate nucleus. *J Neurosci* 25: 3531–3538, 2005. doi:10.1523/JNEUROSCI.4417-04.2005.
11. Lesica NA, Stanley GB. Encoding of natural scene movies by tonic and burst spikes in the lateral geniculate nucleus. *J Neurosci* 24: 10731–10740, 2004. doi:10.1523/JNEUROSCI.3059-04.2004.
12. Reinagel P, Godwin D, Sherman SM, Koch C. Encoding of visual information by LGN bursts. *J Neurophysiol* 81: 2558–2569, 1999. doi:10.1152/jn.1999.81.5.2558.
13. Wang X, Wei Y, Vaingankar V, Wang Q, Koepsell K, Sommer FT, Hirsch JA. Feedforward excitation and inhibition evoke dual modes of firing in the cat’s visual thalamus during naturalistic viewing. *Neuron* 55: 465–478, 2007. doi:10.1016/j.neuron.2007.06.039.
14. Martinez-Conde S, Macknik SL, Hubel DH. The function of bursts of spikes during visual fixation in the awake primate lateral geniculate

- nucleus and primary visual cortex. *Proc Natl Acad Sci USA* 99: 13920–13925, 2002. doi:10.1073/pnas.212500599.
15. **Guido W, Lu SM, Vaughan JW, Godwin DW, Sherman SM.** Receiver operating characteristic (ROC) analysis of neurons in the cat's lateral geniculate nucleus during tonic and burst response mode. *Vis Neurosci* 12: 723–741, 1995. doi:10.1017/s095252380008993.
 16. **Guido W, Lu SM, Sherman SM.** Relative contributions of burst and tonic responses to the receptive field properties of lateral geniculate neurons in the cat. *J Neurophysiol* 68: 2199–2211, 1992. doi:10.1152/jn.1992.68.6.2199.
 17. **Borden PY, Wright NC, Sederberg AJ, Waiblinger C, Haider B, Stanley GB.** Thalamic modulation and the shaping of cortical sensory representations in the awake and anesthetized mouse. *2019 Neuroscience Meeting Planner*. Washington, DC: Society for Neuroscience, 2019. Program No. 221.19.
 18. **Guido W, Weyand T.** Burst responses in thalamic relay cells of the awake behaving cat. *J Neurophysiol* 74: 1782–1786, 1995. doi:10.1152/jn.1995.74.4.1782.
 19. **Estebanez L, Boustani SE, Destexhe A, Shulz DE.** Correlated input reveals coexisting coding schemes in a sensory cortex. *Nat Neurosci* 15: 1691–1699, 2012. doi:10.1038/nn.3258.
 20. **Petersen RS, Brambilla M, Bale MR, Alenda A, Panzeri S, Montemurro M. A, Maravall M.** Diverse and temporally precise kinetic feature selectivity in the VPM thalamic nucleus. *Neuron* 60: 890–903, 2008. doi:10.1016/j.neuron.2008.09.041.
 21. **Ramirez A, Pnevmatikakis E, Merel J, Paninski L, Miller KD, Bruno RM.** The spatiotemporal receptive fields of barrel cortex neurons revealed by reverse correlation of synaptic input. *Nat Neurosci* 17: 866–875, 2014. doi:10.1038/nn.3720.
 22. **Ahissar E, Sosnik R, Haidarliu S.** Transformation from temporal to rate coding in a somatosensory thalamocortical pathway. *Nature* 406: 302–306, 2000. doi:10.1038/35018568.
 23. **Montemurro MA, Panzeri S, Maravall M, Alenda A, Bale MR, Brambilla M, Petersen RS.** Role of precise spike timing in coding of dynamic vibrissa stimuli in somatosensory thalamus. *J Neurophysiol* 98: 1871–1882, 2007. doi:10.1152/jn.00593.2007.
 24. **Chuong AS, Miri ML, Busskamp V, Matthews GAC, Acker LC, Sørensen AT, Young A, Klapoetke NC, Henninger MA, Kodandaramaiah SB, Ogawa M, Ramanlal SB, Bandler RC, Allen BD, Forest CR, Chow BY, Han X, Lin Y, Tye KM, Roska B, Cardin J. A, Boyden ES.** Noninvasive optical inhibition with a red-shifted microbial rhodopsin. *Nat Neurosci* 17: 1123–1129, 2014. doi:10.1038/nn.3752.
 25. **Scheyltjens I, Laram M-E, Van Den Haute C, Gijsbers R, Debyser Z, Baekelandt V, Vreysen S, Arckens L.** Evaluation of the expression pattern of rAAV2/1, 2/5, 2/7, 2/8, and 2/9 serotypes with different promoters in the mouse visual cortex. *J Comp Neurol* 523: 2019–2042, 2015. doi:10.1002/cne.23819.
 26. **Stujenske JM, Spellman T, Gordon JA.** Modeling the spatiotemporal dynamics of light and heat propagation for in vivo optogenetics. *Cell Rep* 12: 525–534, 2015. doi:10.1016/j.celrep.2015.06.036.
 27. **Owen SF, Liu MH, Kreitzer AC.** Thermal constraints on in vivo optogenetic manipulations. *Nat Neurosci* 22: 1061–1065, 2019. doi:10.1038/s41593-019-0422-3.
 28. **Quiroga RQ, Nadasdy Z, Ben-Shaul Y.** Unsupervised spike detection and sorting with wavelets and superparamagnetic clustering. *Neural Comput* 16: 1661–1687, 2004. doi:10.1162/089976604774201631.
 29. **Rossant C, Kadir SN, Goodman DFM, Schulman J, Hunter MLD, Saleem AB, Grosmark A, Denfield GH, Ecker AS, Tolias AS, Solomon S, Buzsáki G, Carandini M, Harris KD.** Spike sorting for large, dense electrode arrays. *Nat Neurosci* 19: 634–641, 2016. doi:10.1038/nn.4268.
 30. **Guo W, Clause AR, Barth-Maron A, Polley DB.** A corticothalamic circuit for dynamic switching between feature detection and discrimination. *Neuron* 95: 180–194.e5, 2017. doi:10.1016/j.neuron.2017.05.019.
 31. **Butts DA, Weng C, Jin J, Yeh C-I, Lesica NA, Alonso J-M, Stanley GB.** Temporal precision in the neural code and the timescales of natural vision. *Nature* 449: 92–95, 2007. doi:10.1038/nature06105.
 32. **Jones JP, Palmer LA.** The two-dimensional spatial structure of simple receptive fields in cat striate cortex. *J Neurophysiol* 58: 1187–1211, 1987. doi:10.1152/jn.1987.58.6.1187.
 33. **Reid RC, Alonso JM.** Specificity of monosynaptic connections from thalamus to visual cortex. *Nature* 378: 281–284, 1995. doi:10.1038/378281a0.
 34. **Eggermont JJ, Johannesma PIM, Aertsen AM.** Reverse correlation methods in auditory research. *Q Rev Biophys* 16: 341–414, 1983. doi:10.1017/s0033583500005126.
 35. **Theunissen FE, Sen K, Doupe AJ.** Spectral-temporal receptive fields of nonlinear auditory neurons obtained using natural sounds. *J Neurosci* 20: 2315–2331, 2000. doi:10.1523/JNEUROSCI.20-06-02315.2000.
 36. **Maravall M, Petersen RS, Fairhall AL, Arabzadeh E, Diamond ME.** Shifts in coding properties and maintenance of information transmission during adaptation in barrel cortex. *PLoS Biol* 5: e19, 2007. doi:10.1371/journal.pbio.0050019.
 37. **Schwartz O, Pillow JW, Rust NC, Simoncelli EP.** Spike-triggered neural characterization. *J Vis* 6: 484–507, 2006. doi:10.1167/6.4.13.
 38. **McFarland JM, Cui Y, Butts DA.** Inferring nonlinear neuronal computation based on physiologically plausible inputs. *PLoS Comput Biol* 9: e1003143, 2013. doi:10.1371/journal.pcbi.1003143.
 39. **Lesica NA, Jin J, Weng C, Yeh C-I, Butts DA, Stanley GB, Alonso J-M.** Adaptation to stimulus contrast and correlations during natural visual stimulation. *Neuron* 55: 479–491, 2007. doi:10.1016/j.neuron.2007.07.013.
 40. **Butts DA, Desbordes G, Weng C, Jin J, Alonso J-M, Stanley GB.** The episodic nature of spike trains in the early visual pathway. *J Neurophysiol* 104: 3371–3387, 2010. doi:10.1152/jn.00078.2010.
 41. **Chagas AM, Theis L, Sengupta B, Stüttgen MC, Bethge M, Schwarz C.** Functional analysis of ultra high information rates conveyed by rat vibrissa primary afferents. *Front Neural Circuits* 7: 190, 2013. doi:10.3389/fncir.2013.00190.
 42. **Goldin M, Harrell E, Estebanez L, Shulz DE.** Rich spatio-temporal stimulus dynamics unveil sensory specialization in cortical area S2. *Nat Commun* 9: 4053, 2018. doi:10.1038/s41467-018-06585-4.
 43. **Maravall M, Alenda A, Bale MR, Petersen RS.** Transformation of adaptation and gain rescaling along the whisker sensory pathway. *PLoS One* 8: e82418, 2013. doi:10.1371/journal.pone.0082418.
 44. **Stanley GB.** Adaptive spatiotemporal receptive field estimation in the visual pathway. *Neural Comput* 14: 2925–2946, 2002. doi:10.1162/089976602760805340.
 45. **Poulet JFA, Crochet S.** The cortical states of wakefulness. *Front Syst Neurosci* 12: 64, 2019. doi:10.3389/fnsys.2018.00064.
 46. **Mukherjee P, Kaplan E.** Dynamics of neurons in the cat lateral geniculate nucleus: in vivo electrophysiology and computational modeling. *J Neurophysiol* 74: 1222–1243, 1995. doi:10.1152/jn.1995.74.3.1222.
 47. **Alitto H, Rathbun DL, Vandeleest JJ, Alexander PC, Usrey WM.** The augmentation of retinogeniculate communication during thalamic burst mode. *J Neurosci* 39: 5697–5710, 2019. doi:10.1523/JNEUROSCI.2320-18.2019.
 48. **Rathbun DL, Alitto HJ, Weyand TG, Usrey WM.** Interspike interval analysis of retinal ganglion cell receptive fields. *J Neurophysiol* 98: 911–919, 2007. doi:10.1152/jn.00802.2006.
 49. **Lesica NA, Weng C, Jin J, Yeh C-I, Alonso J-M, Stanley GB.** Dynamic encoding of natural luminance sequences by LGN bursts. *PLoS Biol* 4: e209, 2006. doi:10.1371/journal.pbio.0040209.
 50. **Waiblinger C, Brugger D, Whitmire CJ, Stanley GB, Schwarz C.** Support for the slip hypothesis from whisker-related tactile perception in a noisy environment. *Front Integr Neurosci* 9: 53, 2015. doi:10.3389/fnint.2015.00053.
 51. **Pinault D.** The thalamic reticular nucleus: structure, function and concept. *Brain Res Brain Res Rev* 46: 1–31, 2004. doi:10.1016/j.brainresrev.2004.04.008.
 52. **Blitz DM, Regehr WG.** Timing and specificity of feed-forward inhibition within the LGN. *Neuron* 45: 917–928, 2005. doi:10.1016/j.neuron.2005.01.033.
 53. **Wang X, Sommer FT, Hirsch JA.** Inhibitory circuits for visual processing in thalamus. *Curr Opin Neurobiol* 21: 726–733, 2011. doi:10.1016/j.conb.2011.06.004.
 54. **Touryan J, Felsen G, Dan Y.** Spatial structure of complex cell receptive fields measured with natural images. *Neuron* 45: 781–791, 2005. doi:10.1016/j.neuron.2005.01.029.
 55. **Sederberg AJ, Pala A, Zheng HJV, He BJ, Stanley GB.** State-aware detection of sensory stimuli in the cortex of the awake mouse. *PLoS Comput Biol* 15: e1006716, 2019. doi:10.1371/journal.pcbi.1006716.

56. **Stoelzel CR, Bereshpolova Y, Swadlow HA.** Stability of thalamocortical synaptic transmission across awake brain states. *J Neurosci* 29: 6851–6859, 2009. doi:10.1523/JNEUROSCI.5983-08.2009.
57. **Swadlow HA, Gusev AG, Bezdudnaya T.** Activation of a cortical column by a thalamocortical impulse. *J Neurosci* 22: 7766–7773, 2002. doi:10.1523/jneurosci.22-17-07766.2002.
58. **Mease RA, Kuner T, Fairhall AL, Groh A.** Multiplexed spike coding and adaptation in the thalamus. *Cell Rep* 19: 1130–1140, 2017. doi:10.1016/j.celrep.2017.04.050.
59. **Desbordes G, Jin J, Weng C, Lesica NA, Stanley GB, Alonso J.** Timing precision in population coding of natural scenes in the early visual system. *PLoS Biol* 6: e324, 2008. doi:10.1371/journal.pbio.0060324.
60. **Gabernet L, Jadhav SP, Feldman DE, Carandini M, Scanziani M.** Somatosensory integration controlled by dynamic thalamocortical feed-forward inhibition. *Neuron* 48: 315–327, 2005. doi:10.1016/j.neuron.2005.09.022.
61. **Crandall SR, Cruikshank SJ, Connors BW.** A corticothalamic switch: controlling the thalamus with dynamic synapses. *Neuron* 86: 768–782, 2015. doi:10.1016/j.neuron.2015.03.040.
62. **Poulet JFA, Fernandez LMJ, Crochet S, Petersen CCH.** Thalamic control of cortical states. *Nat Neurosci* 15: 370–372, 2012. doi:10.1038/nn.3035.
63. **Reinhold K, Lien AD, Scanziani M.** Distinct recurrent versus afferent dynamics in cortical visual processing. *Nat Neurosci* 18: 1789–1797, 2015. doi:10.1038/nn.4153.
64. **Wimmer RD, Schmitt LI, Davidson TJ, Nakajima M, Deisseroth K, Halassa MM.** Thalamic control of sensory selection in divided attention. *Nature* 526: 705–709, 2015. doi:10.1038/nature15398.
65. **Bolus MF, Willats AA, Rozell CJ, Stanley GB.** State-space optimal feedback control of optogenetically driven neural activity. *J Neural Eng*, 18: 036006, 2021. doi:10.1088/1741-2552/abb89c.
66. **Bolus MF, Willats AA, Whitmire CJ, Rozell CJ, Stanley GB.** Design strategies for dynamic closed-loop optogenetic neurocontrol in vivo. *J Neural Eng* 15: 026011, 2018. doi:10.1088/1741-2552/aaa506.
67. **Newman JP, Fong M-F, Millard DC, Whitmire CJ, Stanley GB, Potter SM.** Optogenetic feedback control of neural activity. *eLife* 4: 07192, 2015. doi:10.7554/eLife.07192.